International Journal of Multiphase Flow 71 (2015) 98–115

Contents lists available at ScienceDirect

International Journal of Multiphase Flow

journal homepage: www.elsevier.com/locate/ijmulflow

Froude number dominates condensation heat transfer of R245fa in tubes: Effect of inclination angles

Feng Xing, Jinliang Xu *, Jian Xie, Huan Liu, Zixuan Wang, Xiaolin Ma

The Beijing Key Laboratory of Multiphase Flow and Heat Transfer, North China Electric Power University, 102206 Beijing, China

ARTICLE INFO

Article history:
Received 20 May 2014
Received in revised form 19 January 2015
Accepted 20 January 2015
Available online 31 January 2015

Keywords:
Condensation heat transfer
Flow pattern
Interface wave
Inclination angle
Organic Rankine Cycle

ABSTRACT

Condensation heat transfer of R245fa in a tube with the diameter of 14.81 mm and length of 1200 mm was investigated. The R245fa mass fluxes, inlet vapor mass qualities and inclination angles covered the ranges of 191.3–705.4 kg/m^2 s, 0.191–0.947 and −90° to 90°, respectively. The non-dimensional analysis yielded the importance of inertia force and gravity force to influence condensation heat transfer. Surface tension force played unimportant role. Condensation heat transfer coefficients (h) showed the general increase trend versus inclination angles (θ) and the non-monotonic behavior in the full inclination angle range. The maximum h occurred at θ = 30° and −15°. The h values were sensitive to θ near the horizontal positions. The main flow patterns in the condenser tube were stratified-smooth flow, stratified-wavy flow and intermittent flow. For inclined upflow, the liquid layer thickness and interface wave competed with each other to influence heat transfer. An optimal inclination angle existed at which heat transfer coefficients reached maximum. For inclined downflow, condensation heat transfer was balanced by the liquid layer thickness and buoyancy force. The flow was more stable. Heat transfer coefficients were well correlated with the general increase term multiplied by the non-monotonic variation term. The parameters in the correlation depended on the Froude number and vapor mass qualities. The correlation successfully explained the effects of mass fluxes, vapor mass qualities and inclination angles on condensation heat transfer coefficients. Based on the present finding, the condenser is recommended to operate at the inclination angle of −15° or 30°, at which heat transfer coefficients are maximum and pressure drops are minimum. The exactly horizontal flow weakens the condenser performance.

Introduction

In-tube condensation heat transfer of refrigerants has been widely investigated. The topic is important to increase the energy efficiency, save space and material for air-conditioning, refrigeration, automotive and process industries. The use of more environmentally friendly refrigerants has further been emphasized (Dalkilic and Wongwises, 2009; Lips and Meyer, 2011). In several studies of convective condensation heat transfer in the last decade, various flow pattern maps and correlations have been developed to predict pressure drops and heat transfer in two-phase heat exchangers with horizontal position. Saffari and Naziri (2010) noted that the development of technology requires a more compact and efficient heat exchanger for application in industries where condensation takes place inside inclined tubes, such as in liquefaction plants, air conditioners, and recently developed heat pipes and solar collectors. Under some circumstances, the inclined condensers are necessary to vent the condensed liquid out of the condenser (Caruso et al., 2013). However, the detailed studies with respect to inclination angles were less reported in the literature. Due to different working fluids and operating parameters, some conclusions were even contradictory with each other. The effect of tube inclination angles on the condensation heat transfer should be further investigated.

The tubes with small diameter were widely used for in-tube condensation heat transfer, as required by the applications of air-conditioning heat exchangers. The typical copper tube had the inner diameter of 8 mm. For two-phase flow in tubes, both gravity force and tube diameter could influence the condensation heat transfer. Gupta et al. (2010) commented on the non-dimensional parameters in two-phase systems, such as Reynolds number (the inertia force relative to viscous force), the Froude number (the inertia force relative to gravity), the Bond number (the gravity force relative to surface tension), the capillary number (the viscous force relative to surface tension), and the Weber number (the inertia force relative to surface tension). In these dimensionless parameters, gravity force is involved in the Froude number and

* Corresponding author. Tel.: +86 10 61772613.
E-mail address: xjl@ncepu.edu.cn (J. Xu).

http://dx.doi.org/10.1016/j.ijmultiphaseflow.2015.01.005
0301-9322/

Bond number. The tube diameter is involved in all the dimensionless parameters except the capillary number. Tilting the tubes influences the gravity force acting on the two-phase flow stream. Thus, flow patterns are strongly dependent on the inclination angles, so as to affect the condensation heat transfer. Usually, the condensation flow patterns include stratified flow (including stratified-smooth and stratified-wavy), intermittent flow (slug flow or plug flow) and annular flow. In small diameter tubes, the importance of surface tension force is enhanced but the gravity force effect is weakened, therefore, the intermittent flow regime is enlarged but the stratified flow regime is narrowed (Hajal et al., 2003; Yang and Shieh, 2001; Weisman et al., 1979).

Lips and Meyer (2012a) measured the flow patterns and heat transfer during convective condensation of R134a in a tube with inner diameter of 8.38 mm. The test section was positioned from vertical downflow to vertical upflow. The mass fluxes and average vapor mass qualities ranged from 200 to 600 kg/m^2 s and from 0.1 to 0.9, respectively. The stratified-wavy flow was dominant at low mass fluxes and vapor mass qualities, under which the heat transfer was sensitive to inclination angles. However, the heat transfer was insensitive to inclination angles when the annular flow was dominant at high mass fluxes and vapor mass qualities. They found that for inclined upflow, the condensation heat transfer coefficients were decreased and then increased versus inclination angles. For inclined downflow, the condensation heat transfer coefficients were increased and then decreased with increasing inclination angles. The condensation heat transfer coefficients reached maximum for downward flow at $\theta = -15°$ to $-30°$ and minimum for upward flow at $\theta = 15°$ Mohseni et al. (2013) investigated flow patterns and heat transfer of R134a in a tube with 8.38 mm in diameter, they found that the condensation heat transfer coefficients reached maximum at $\theta = 30°$ (upflow) for low vapor mass qualities but reached maximum at the horizontal position with high vapor qualities. It is seen that the conclusions of Mohseni et al. (2013) are quite different from those of Lips and Meyer (2012a). It is noted that condensation heat transfer coefficients are influenced by flow patterns and interface waves, which are relied on the working fluid used, geometry configuration and size, running parameters of heat fluxes, mass fluxes and vapor mass qualities. These factors may be accounted for different conclusions drawn by different authors (Mohseni et al., 2013). Saffari and Naziri (2010) studied the condensation heat transfer in a tube of 14.3 mm in diameter for inclined downflow. They found that the condensation heat transfer coefficients were increased and then decreased versus inclination angles. The maximum value occurred at $\theta = -30°$ to $-50°$.

Lips and Meyer (2012b) modified the classical stratified flow model during condensation. The liquid–vapor interface was assumed as curve surface instead of the classical flat surface assumption. A hydraulic and heat transfer model was developed by balancing the gravity force and capillary force. Thus, the liquid–vapor interface shape and location were captured to approach the realistic situation. The model predictions were consistent with the experimental data. Wang and Du (2000) developed a liquid film condensation heat transfer model for downward flow. The model predictions deviated from the experimental data by −28% to 20%. Wang et al. (1998) developed a flow pattern map for condensation of R11 in a 6 mm diameter copper tube. The inclination angles were changed from the vertical downflow to the vertical upflow. The flow pattern maps were plotted with the two-phase Weber numbers as the coordinates.

In addition to applications in air-conditioning and refrigeration systems, condensation heat transfer is widely used for low grade energy and renewable energy utilizations. An Organic Rankine Cycle (ORC) converts low grade heat to power (Wei et al., 2007; Madhawa et al., 2007; Schuster et al., 2009). The organic liquid (such as R245fa) is heated to produce vapor, driving the turbine to generate power. The venting vapor at the turbine outlet is condensed and circulated by a pump. A heat pump with evaporator and condenser is another system to use the low grade thermal energy. The condenser tube diameters are usually larger than those used for air-conditioning industries.

Due to the great interest to use low grade energy and renewable energy, it is necessary to investigate condensation heat transfer in larger diameter tubes. Meanwhile, the working fluid of R245fa was believed to have better thermodynamic cycle performance than other organic fluids (Kang, 2012; Wang et al., 2011), but the condensation heat transfer data of R245fa were less reported in the literature. The above consideration encouraged us to perform this study. Because of the lower surface tension force of R245fa than water and relative larger tube diameter, the surface tension force has less effect on the condensation heat transfer, comparatively, the inertia force and gravity force become more important, leading to the narrower intermittent flow regime and the larger stratified flow regime.

The interface wave effect on the condensation heat transfer was often neglected in small diameter tubes (Wang and Du, 2000), however, the interface wave may be accompanied by the stratified flow to decrease the liquid film thickness (Frisk and Davis, 1972). Meanwhile, the re-circulating flow occurs in the peak region of the large amplitude wave (Jayanti and Hewitt, 1996), thus condensation heat transfer mechanism in larger diameter tubes may be different from that in small diameter tubes.

The objective of this paper was to investigate the in-tube condensation heat transfer of organic fluid. The effect of inclination angles was studied thoroughly. The structure of this paper was organized as follows. Section 'The experimental details and data reduction' described experimental details. Section 'Results and discussions' presented results and analysis. Sections 'Effect of vapor mass qualities and mass fluxes' and 'Effect of inclination angles' reported condensation heat transfer coefficients influenced by mass fluxes, vapor mass qualities and inclined angles. Section 'The flow patterns and interface wave' described flow patterns and interface waves. Section 'Explanation of the observed data trend and phenomena' focused on the explanation of the observed phenomena. This section started from the non-dimensional parameter analysis, showing the importance of inertia force and gravity force and related Froude number. Then flow patterns and interface waves were explained by the dimensionless parameter. The logical connection among condensation heat transfer coefficients, flow patterns and interface waves were explored. Section 'The two-step correlation of h with respect to θ' gave the correlation of condensation heat transfer coefficients. The physical meaning of parameters in the correlation was discussed. The conclusions were summarized in section 'Conclusions'.

The experimental details and data reduction

Experimental loop

The experimental setup consisted of an organic fluid loop, an evaporator, a test section, a chiller water loop, a tap water cooled post-condenser and relevant instruments (see Fig. 1). The R245fa fluid was circulated by a diaphragm pump, ensuring that the R245fa fluid did not contain any oil droplet. Initially the non-condensable gas was removed from the organic fluid loop and then the R245fa liquid was charged into the loop. A pump flow rate was specified by setting the pump frequency and diaphragm displacement. The fluid pressure was stabilized by an accumulator at the pump outlet. The nitrogen gas pressurized the liquid level of the accumulator.

A helical-coiled tube was used as the evaporating section, heated by an *AC* (alternative current) electrical power. The high

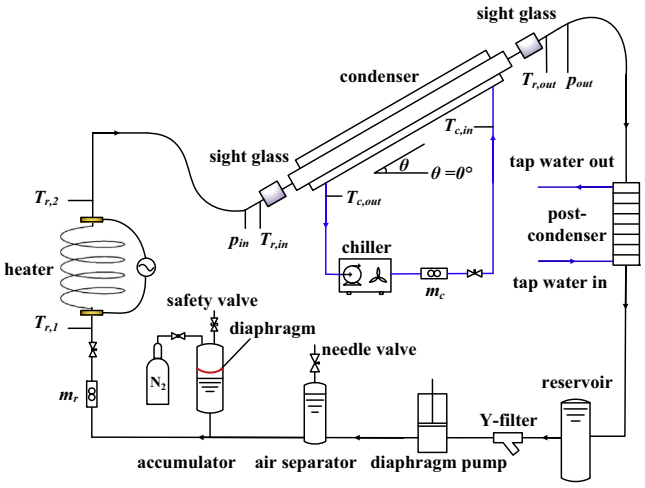

Fig. 1. The experimental setup.

AC voltage was converted to low *AC* voltage by a transformer converter. The evaporator was electrically insulated with other components of the loop. Two copper plates were welded on the curved tube and acted as the electrodes. The curved tube was wrapped by thick thermal insulation material. The voltage and current were measured to obtain the power value. The evaporator had the subcooled liquid at the inlet, with the temperature recorded as $T_{r,1}$. The outlet temperature was $T_{r,2}$, which equals to the fluid saturation temperature with the two-phase mixture at the outlet. In order to investigate the effect of inclination angles on the condensation heat transfer, a special test rig was fabricated to have the rotating function. The test section was tightly bonded with the test rig. The inclination angles had the uncertainty of 0.5°.

The chiller water loop condensed the two-phase mixture in the test section. The loop included a chiller, a mass flow meter and two jacket thermocouples. The chiller generated a stable chiller water flow rate, m_c, measured by a mass flow meter. The heat was dissipated by a fan to the ambient air. The inlet and outlet temperatures of the chiller water were measured by two thermocouples ($T_{c,in}$ and $T_{c,out}$). For many cases the vapor was set not to be fully condensed at the test section outlet. Thus the vapor mass qualities had acceptable difference across the condenser inlet and outlet, under which one can identify the effect of vapor mass qualities on condensation heat transfer coefficients. The outlet mixture was further condensed to subcooled liquid by a post-condenser, with the tap water flowing inside.

Test section

The test section was a counter-current condenser (see Fig. 2), consisting of two sight glass tube adaptors, an inner copper tube and an outer stainless steel tube. The R245fa mixture was flowing in the copper tube. The cooling water was flowing in the tube annulus between the stainless tube and the copper tube. Two flanges connected the copper tube and the sight glass tube together. The outside and inside diameters of the copper tube were d_o = 18.97 mm and d_i = 14.81 mm, respectively. The effective heat transfer length was 1200 mm. The 304 stainless steel tube had an inner diameter of D_i = 23.80 mm, forming a tube annulus of 2.42 mm for the cooling water channel. The sight glass tube was used for the high speed flow visualization. Pressure and temperature sensors were arranged at the test section inlet and outlet, respectively.

Seven cross sections were marked as 1–7. The distance between two neighboring cross sections was 200 mm. The cross section 1 was for the organic fluid inlet and cross section 7 was for the outlet, respectively (see Fig. 2b). Four branch tubes were welded with the outer stainless steel tube to vent the cooling water in the tube annulus. Three thermocouple wires were welded on the top, side and bottom wall locations and they penetrated the corresponding branch tube for signal processing. A jacket thermocouple in the branch tube measured the cooling water temperature.

Usually, the vapor and liquid phases are non-uniformly distributed over the tube cross section for inclined tube. Vapor is lighter thus it tends to be populated at the tube top. But liquid is heavier thus it tends to be at the tube bottom. The non-uniform phase distribution yields the non-uniform temperature distribution. Therefore, we used three thermocouples on the tube wall at each cross section to detect the varied temperatures. Similar method was also used by Son and Oh (2012) and Lee et al. (2006).

For the cross sections 2–6, three thermocouples on the tube wall were marked as $T_{i,w,t}$, $T_{i,w,s}$ and $T_{i,w,b}$, where i and w referred to the cross section number (i = 2–6) and the wall, t, s and b referred to the top, side and bottom locations, respectively. $T_{i,c}$ measured the cooling water temperature in the tube annulus with c standing for the cooling water (see Fig. 2c).

Totally 375 runs were performed. The R245fa mass fluxes (G) and inlet vapor mass qualities (x_{in}) covered the range of 191.3–705.4 kg/m^2 s and 0.191–0.947, respectively. The inclination angles were in the range of −90° to 90°, in which θ = 0° referred to the horizontal flow, θ = −90° and 90° referred to the vertical downflow and vertical upflow, respectively. The typical heat duties were in the range of 1.16–4.34 kW, the cooling water temperature differences, ΔT, were in the range of 2.0–7.4 °C. Table 1 summarizes the major operating parameters in this study.

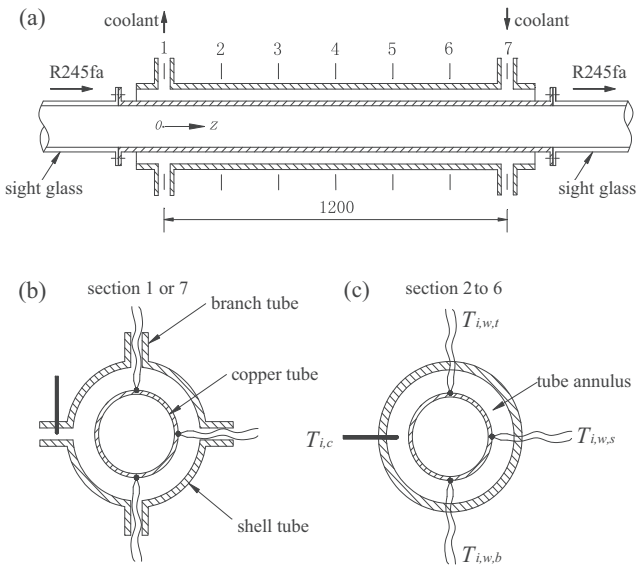

Fig. 2. The condenser tube test section.

Table 1
The experimental running parameters.

Parameters	Range
Mass flux, G	191.3–705.4 kg/m^2 s
Inlet vapor temperature, $T_{r,in}$	55.4 ± 0.3 °C
Inlet vapor pressure, p_{in}	404.9 ± 3.0 kPa
Inlet vapor mass quality, x_{in}	0.191–0.947
Heat duties of test section, Q	1.16–4.34 kW
Heat flux on the inner side wall, q	21.24–79.32 kW/m^2
Cooling water mass flow rate, m_c	500.0 ± 0.5 kg/h
Cooling water inlet temperature, $T_{c,in}$	25.1 ± 0.3 °C
Cooling water temperature difference, ΔT	2.0–7.4 °C
Inclination angle, θ	−90° to 90°

The studied fluid was R245fa, which is non-flammable and non-toxic. The fluid has zero ODP (Ozone Depletion Potential). It represents a substitute for HCFC-123 and CFC-11 refrigerants. The literature survey noted that R245fa has great potential to be used in Organic Rankine Cycles for power generation. The cycle with R245fa has high thermal efficiency and ensures the dry expansion in the turbine.

In order to observe flow patterns, a glass tube with its inside diameter exactly identical to that for the heat transfer measurement was used. That is to say, flow patterns were directly recorded in a glass tube without an outer shell tube. It is noted that flow patterns in the glass tube under the adiabatic condition are somewhat different from those in the copper tube under the diabatic (heat transfer) condition. The wall roughness and thermal conductivity may cause the deviation in the two different tubes. However, Taitel and Dukler (1976) noted that the phase distribution of the two-phases such as the liquid height in the tube are mainly influenced by the mass fluxes, vapor mass qualities, thermopysical properties of the working fluids and shear stress on the tube wall. The wall shear stress is influenced by the wall roughness only when the flow is in the turbulent-roughed flow region (Nikuradse, 1950). Our experiment covered the turbulent-smooth flow region, which minimized the flow pattern difference between glass tube and copper tube.

Kattan et al. (1998) compared flow patterns under adiabatic and diabatic conditions. Fig. 11 in Kattan et al. (1998) shows that the transition boundaries among stratified-smooth flow (*SS*), stratified-wavy flow (*SW*), intermittent flow (*I*) are the same for adiabatic and diabatic conditions. The predicted mass fluxes at the transition boundaries among these flow patterns did not contain the heat flux, indicating no influence of heat transfer on these flow patterns (Kattan et al., 1998). The heat flux only affects the formation of annular flow at high vapor quality. In this study, the *SS*, *SW* and *I* flow patterns are paid much attention. It is concluded that the flow patterns recorded through glass tube can represent those in the copper tube, when the tube diameter and running parameters are the same in the two tubes. Less attention was paid to the annular flow. Because flow patterns are difficult to be obtained in the copper tube, flow patterns obtained through glass tube are widely used by other investigators such as Lips and Meyer (2012a) and Lee et al. (2006).

The removal of non-condensable gas in R245fa

It is difficult to directly measure the non-condensable gas concentration, but we calculate the gas concentration in R245fa based on Henry's law: $S_{gas} = k_H p_{gas}$, where S_{gas} is the gas solubility, k_H is the Henry's constant, p_{gas} is the gas pressure which is $p_{gas} = p - p_v$, p is the pressure in the condenser tube of this study. The Henry's constant k_H is evaluated based on the correlation of Vinš and Hrubý (2011). For the test case of $G = 498.4$ kg/m^2 s and $x_{in} = 0.40$ of this study, the measured pressure and temperature were 402.9 kPa and 55.2 °C, respectively. Our estimation yielded the mole fraction of air in R245fa was 9.75×10^{-6}, corresponding to the volume fraction of air in R245fa liquid of 6.08×10^{-4}. On the other hand, the volume fractions of air in water at the atmospheric pressure were 2.918×10^{-3} and 1.868×10^{-3} at the temperatures of 0 °C and 20 °C, respectively. It is seen that the solubility of air in R245fa liquid is about one third of that of air in water.

In addition to the above estimation, the following measures were taken: (1) The non-condensable gas was vacuumed from the experimental loop before charging R245fa liquid. (2) The R245fa liquid was separated from nitrogen gas by a flexible diaphragm in the liquid accumulator. Thus, the R245fa fluid and gas did not contact with each other (see Fig. 1). (3) Fig. 1 shows a long non-condensable gas venting tube positioned vertically at the pump outlet. Before the formal experiment, the convective flow was established. The voltage heating was applied to the R245 liquid by the helical coiled tube. The non-condensable gas can be released from the liquid due to heating. The released gas was accumulated in the venting tube. After a couple of hours' operation, the safety valve at the venting tube top was manually opened to discharge gas to environment. After the continuous operation of the loop, when pure liquid without any gas was discharged, it was assured that the non-condensable gas was thoroughly removed.

The negligible gas in R245fa liquid can also be verified by the corresponding relationship of vapor pressure and temperature. Table 1 shows the parameters at the test section inlet. For example, the saturation pressure was 408.4 kPa at the measured temperature of 55.7 °C, while the measured pressure was 407.9 kPa. The two pressure values deviated from each other only by 0.122%, which is acceptable for the experiment.

Calibration experiment

The single-phase R245fa flow and heat transfer experiments were performed to obtain the evaporator and condenser efficiencies. The evaporator thermal efficiency was

$$\eta_h = \frac{m_r C_{p,r}(T_{r,2} - T_{r,1})}{UI} \tag{1}$$

where m_r was the R245fa mass flow rate, $C_{p,r}$ was the specific heat of R245fa liquid, $T_{r,2}$ and $T_{r,1}$ were the liquid temperatures at the evaporator outlet and inlet respectively, U was the voltage and I was the current. The measured evaporator thermal efficiency was about 0.97.

Then, the condenser thermal efficiency (organic fluid side), η_{con}, was

$$\eta_{con} = \frac{m_c C_{p,c}(T_{c,out} - T_{c,in})}{m_r C_{p,r}(T_{r,in} - T_{r,out})} \tag{2}$$

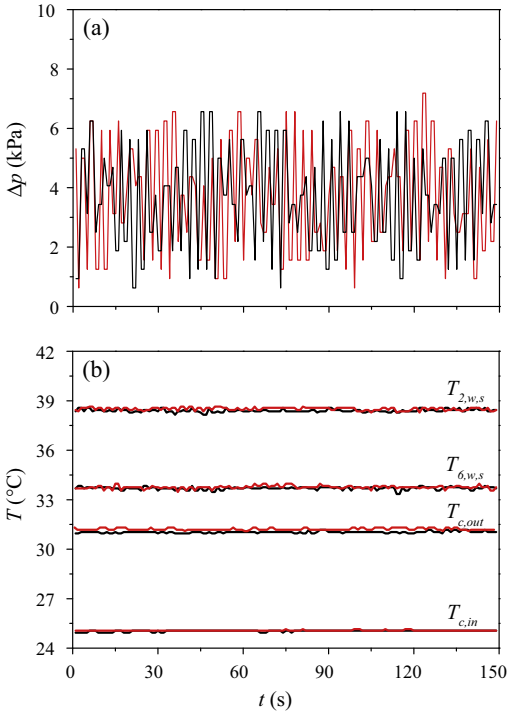

Fig. 3. Repeatable experiment for a typical case (the black and red curves were obtained on the first day and second day respectively, the data recording rate was 1 Hz, $G = 398.8$ kg/m^2 s, $x_{in} = 0.506$, $x_{out} = 0.211$, $\theta = 0°$). (For interpretation of the references to colour in this figure legend, the reader is referred to the web version of this article.)

where m_c was the cooling water mass flow rate, $C_{p,c}$ was the water specific heat, $T_{c,out}$ and $T_{c,in}$ were the outlet and inlet water temperatures, respectively. The measured η_{con} reached about 0.98.

The friction factors and Nusslet number of R245fa liquid in the tube were measured. The friction factors in turbulent flow regime agreed well with those computed by the Blasius expression (Tropea et al., 2007), with the relative difference less than 6%. The Nusselt number also matched the Dittus–Boelter correlation (Dittus and Boelter, 1985), with the relative difference less than 5%.

Data reduction and uncertainty analysis

Inlet and outlet vapor mass qualities (x_{in} and x_{out})

The evaporator parameters and the efficiency, η_h, yielded the condenser inlet enthalpy ($i_{r,in}$) and quality (x_{in}), see section 'Calibration experiment':

$$i_{r,in} = i_{r,1} + \frac{UI\eta_h}{m_r} \tag{3}$$

$$x_{in} = \frac{i_{r,in} - i_{f,in}}{i_{fg,in}} \tag{4}$$

where $i_{r,1}$ is the R245fa enthalpy at the evaporator inlet, $i_{f,in}$ and $i_{fg,in}$ are the saturated liquid enthalpy and latent heat of evaporation based on the inlet pressure, respectively.

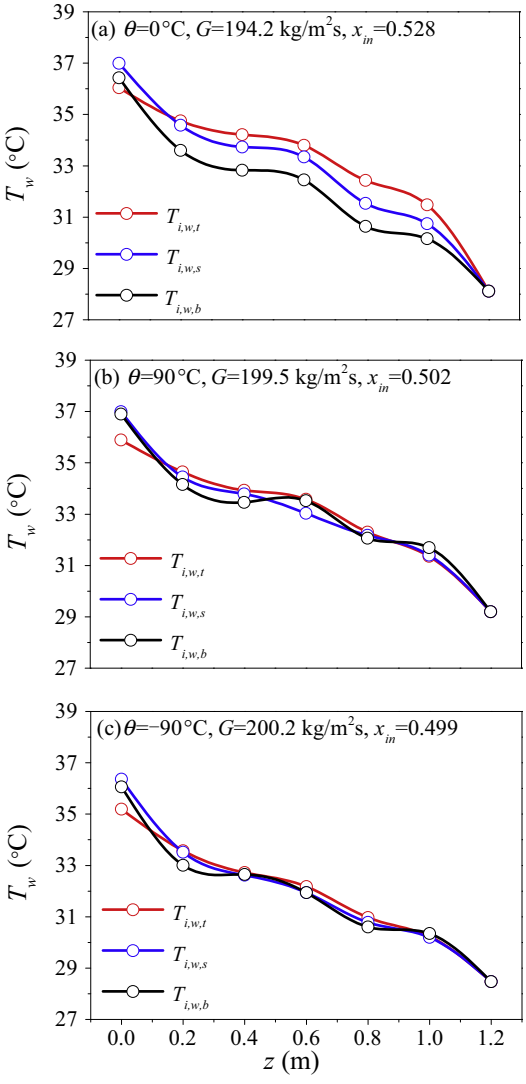

Fig. 4. Variation in wall temperature circumferentially and axially at inclination of 0° and ±90°.

The condenser outlet parameters were computed in terms of the condenser efficiency (η_{con} in Eq. (2)). The heat received by the cooling water in the tube annulus was

$$Q = m_c C_{p,c}(T_{c,out} - T_{c,in}) \tag{5}$$

The heat flux based on the inner tube wall surface of the copper tube was

$$q = Q/(\pi d_i L_{con}) \tag{6}$$

where L_{con} is the effective heat transfer length. The outlet vapor enthalpy and quality were

$$i_{r,out} = i_{r,in} - \frac{Q}{m_r \eta_{con}} \tag{7}$$

$$x_{out} = \frac{i_{r,out} - i_{f,out}}{i_{fg,out}} \tag{8}$$

where $i_{f,out}$ and $i_{fg,out}$ are the saturated liquid enthalpy and latent heat of evaporation based on the outlet pressure, respectively.

Heat transfer coefficients

The average vapor mass quality x_{ave} in the copper tube was $x_{ave} = 0.5(x_{in} + x_{out})$. The condensation heat transfer coefficient h was (Laohalertdecha and Wongwises, 2010):

$$h = \frac{1}{\frac{1}{h_{to}} - \frac{d_i}{2k_w}\ln\left(\frac{d_o}{d_i}\right) - \frac{d_i}{d_o}\frac{1}{h_c}} \tag{9}$$

where k_w was the thermal conductivity of the stainless steel tube. The total heat transfer coefficient h_{to} in Eq. (9) was

$$h_{to} = \frac{q}{LMTD} \tag{10}$$

In which q was predicted by Eqs. (5) and (6), the LMTD temperature difference was

$$LMTD = \frac{(T_{r,in} - T_{c,out}) - (T_{r,out} - T_{c,in})}{\ln\left(\frac{T_{r,in} - T_{c,out}}{T_{r,out} - T_{c,in}}\right)} \tag{11}$$

$$h_c = \frac{q d_i}{d_o(T_{w,ave} - T_{c,ave})} \tag{12}$$

$T_{w,ave}$ and $T_{c,ave}$ are the average temperatures of the tube wall and the cooling water, which are

$$T_{w,ave} = \frac{1}{3n}\sum_{i=1}^{n} T_{i,w,t} + T_{i,w,s} + T_{i,w,b}, \quad T_{c,ave} = \frac{1}{n}\sum_{i=1}^{n} T_{i,c} \tag{13}$$

The subscripts t, s and b refer to the top, side and bottom wall (see Fig. 2c), i is the cross section number, n equal to 7 here. The total pressure drop of R245fa across the condenser was $\Delta p = p_{in} - p_{out}$.

Uncertainty analysis

High accuracy sensors and instruments were used. The temperatures measured by OMEGA K-type thermocouples had the uncertainty of 0.1 °C after careful calibration. The mass flow rate was measured by DMF-1-DX mass flow meters, having the uncertainty of 0.1%. Both the *AC* voltage and current had the uncertainties of 0.1%. We used the data acquisition system with the chassis model number of NI PXIe-1062Q. The chassis had eight slots, each having a specific bandwidth with the speed of 1 GB/s and a system bandwidth with the speed exceeding 3 GB/s. The NI PXIe-4353 temperature module and the NI TB-4353 junction box were used for the temperature measurements. The temperature accuracy was 0.05 °C due to the temperature module and data acquisition system used. The NI-PXI-6251 module was used for the voltage measurement with the accuracy of 0.01% and the sampling rate up to 1.25 M samples per second. Uncertainties of vapor mass qualities and heat transfer coefficient were evaluated in terms of

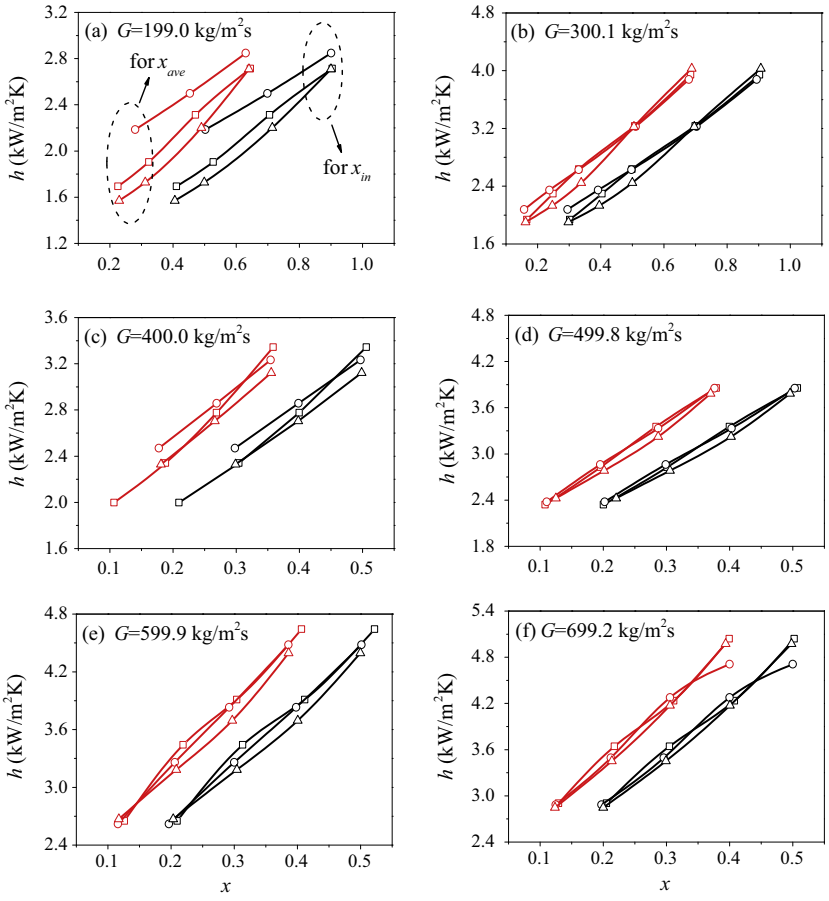

Fig. 5. Condensation heat transfer coefficient versus vapor mass qualities (red symbols for h–x_{ave} and black symbols for h–x_{in}, □ for $\theta = 0°$, ○ for $\theta = 90°$, Δ for $\theta = -90°$). (For interpretation of the references to colour in this figure legend, the reader is referred to the web version of this article.)

the error transmission theory (Holman and Gajda, 1994). If Y is a given function of the independent variables of $\tilde{x}_1, \tilde{x}_2, \tilde{x}_3 \ldots \tilde{x}_n$ and $\Delta\tilde{x}_1, \Delta\tilde{x}_2, \Delta\tilde{x}_3 \ldots \Delta\tilde{x}_n$ are the uncertainties of these independent parameters, the uncertainty of Y is

$$\Delta Y = \sqrt{\left(\frac{\partial Y}{\partial \tilde{x}_1}\Delta\tilde{x}_1\right)^2 + \left(\frac{\partial Y}{\partial \tilde{x}_2}\Delta\tilde{x}_2\right)^2 + \ldots \left(\frac{\partial Y}{\partial \tilde{x}_n}\Delta\tilde{x}_n\right)^2} \quad (14)$$

The heat transfer coefficient (h), vapor mass qualities (x) and heat fluxes (q) had the accuracies of 4.85%, 5.93% and 5.81%, respectively. The rotating angles had the accuracy of 0.5°.

Results and discussions

Before we presented the condensation heat transfer coefficient data, we repeated the experiments for the same running parameters at different time. This verified the usefulness of the test loop and the correctness of the data. During the phase change process, parameters may be oscillating versus time due to the two-phase flow instability. An orifice restrictor was put at the evaporator inlet so that the two-phase flow instability was suppressed to reach the quasi-steady operation. Fig. 3 shows the repeatable two-phase measurements for $G = 398.8$ kg/m^2 s and $x_{in} = 0.506$. The black and red curves were obtained on the first day and second day, respectively. It is seen that the test was repeatable. The repeatable test further verified that the non-condensable gas effect can be neglected during the running of the test loop. The pressure drop signal was oscillating with the average value of about 4 kPa (see Fig. 3a). However, the inlet and outlet cooling water temperatures ($T_{c,in}$ and $T_{c,out}$) were very stable, the wall temperatures $T_{2,w,s}$ and $T_{6,w,s}$ (cross sections 2 and 6 for side wall location) were stable with the oscillating amplitude in a narrow range of 0.1–0.2 °C (see Fig. 3b). This was because the thermal inertia of the copper tube wall flattened the temperature oscillations. All the 21 wall temperatures were involved in the heat transfer coefficient computation, and the data was averaged over a long time period of several minutes. The hardware arrangement and data processing procedure ensured the experimental data reliability. It is noted that the pressure drop oscillation was dependent on flow patterns. Processing the pressure drop oscillation data can yield the flow pattern information, which was beyond the scope of this paper.

Fig. 4 shows wall temperatures along flow direction with $G \approx 200$ kg/m^2 s and $x_{in} \approx 0.5$. The condenser tube had a counter-current flow of R245fa mixture in the tube and water in the tube annulus (see Fig. 2). The R245fa mixture was continuously condensed along flow direction with cooling water entering the tube annulus at $z = 1.2$ m. Thus, wall temperatures were continuously decreased along flow direction. Fig. 4a shows wall temperatures for horizontal position. The horizontal flow caused non-uniform phase distribution over tube cross section. Vapor is lighter thus it tends to accumulate at the tube top. But liquid is heavier thus it tends to accumulate at the tube bottom. Such phase distribution yielded higher condensation heat transfer coefficients at tube top than those at tube bottom. Therefore, Fig. 4a shows highest wall temperatures at tube top ($T_{i,w,t}$) and lowest wall temperatures at tube bottom ($T_{i,w,b}$) at each cross section. The side locations had wall temperatures between top and bottom locations. Fig. 4b and c show wall temperatures for vertical upflow and vertical downflow, respectively. For both cases the flow was uniform over the tube cross section. Thus, there is no apparent difference of wall

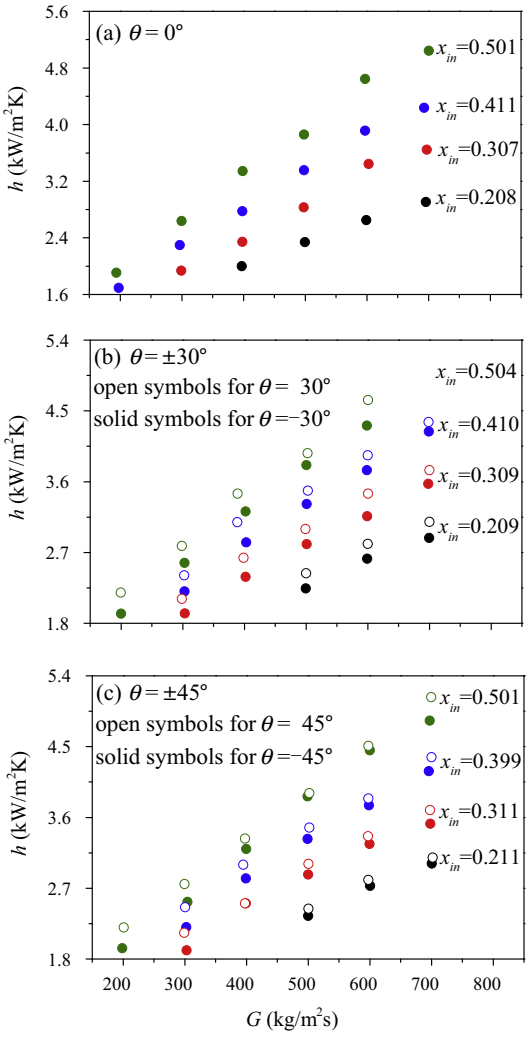

Fig. 6. The condensation heat transfer coefficients versus mass fluxes.

temperatures among the three locations for $\theta = 90°$ and $-90°$. The wall temperatures at the water inlet ($z = 1.2$ m) were almost the same for the three subfigures, due to the entrance effect.

Effect of vapor mass qualities and mass fluxes

Fig. 5 shows the condensation heat transfer coefficients versus vapor mass qualities at six mass fluxes. The red symbols and curves are for h versus x_{ave}, and black symbols and curves are for h versus x_{in}. The circular, rectangular and triangular symbols are the h data obtained at $\theta = 90°$, 0° and $-90°$, respectively. It was observed that h was increased quasi-linearly with increases in x_{in} or x_{ave}. Larger vapor mass qualities increased the velocities of both liquid and vapor phases and reduced the liquid film thickness on the wall to increase the heat transfer coefficients. The slopes of h with respect to x were increased with increasing mass fluxes (see Fig. 5a–f), noting that the x ranges are from 0 to 1.0 in Fig. 5a and b and from 0 to 0.5 in Fig. 5c–f. This indicated that the condensation heat transfer coefficients were more sensitive to vapor mass qualities at high mass fluxes. The heat transfer coefficients are obviously different at the three inclination angles at $G = 199.0$ kg/m^2 s, but the effect of inclination angles on h are complicated and will be presented in following figures.

Fig. 6 shows the condensation heat transfer coefficients versus mass fluxes. The curve of h–G also behaved a quasi-linear way. Fig. 6b and c identified that the inclined upflow behaved a slight larger heat transfer coefficients than the inclined downflow. The h difference at $\theta = \pm 30°$ (see Fig. 6b) was larger than that at $\theta = \pm 45°$ (see Fig. 6c). Figs. 5 and 6 observed the increased condensation heat transfer coefficients with both vapor mass qualities and mass fluxes.

Effect of inclination angles

Fig. 7 identifies the effect of inclination angles on the condensation heat transfer at six mass fluxes and various vapor mass qualities. In order to clearly see the inclination angle effect, $h/h_{\theta=0}$ was defined as the condensation heat transfer coefficient at any inclination angle divided by that at the horizontal position (see Fig. 8). The following phenomena were observed: (a) *The deviation of h from that at θ = 0:* The condensation heat transfer coefficient can be different from that at the horizontal position. For the data shown in Fig. 8, h can be 16% larger than $h_{\theta=0}$, and 12% lower than $h_{\theta=0}$, maximally. (b) *The increase trend of $h/h_{\theta=0}$ versus θ:* Generally, $h/h_{\theta=0}$ had a increasing trend with the inclination angles from $-90°$ to 90°. The increasing trend was more dramatic at low mass fluxes such as $G < 400$ kg/m^2 s, and it became weakened at large mass fluxes. (c) *The non-monotonic behavior of $h/h_{\theta=0}$ versus θ:* The $h/h_{\theta=0}$ values exhibited the non-monotonic behavior against the inclination angles covering the range of ($-90°$ to 90°). For the inclined upward flow with $0 < \theta < 90°$, the maximum $h/h_{\theta=0}$ always occurred at about $\theta = 30°$. For the inclined downward flow with $-90° < \theta < 0°$, the maximum $h/h_{\theta=0}$ occurred at $\theta = -15°$.

The general increasing trend and the non-monotonic behavior indicted the complicated condensation of R245fa in a larger diameter tube than 8 mm. In this study it was found the condensation heat transfer coefficients were sensitive to the inclination angles near horizontal positions. Fig. 9 focused the condensation heat transfer ratio of $h/h_{\theta=0}$ in a narrow range of inclination angles ($-15°$ to 15°). Either slightly inclined upflow or inclined downflow had larger condensation heat transfer coefficients than the exactly horizontal flow.

The flow patterns and interface wave

We presented flow patterns and interface wave experiments here. The visualization experiments are to explore condensation heat transfer mechanism varied with inclination angles.

The flow patterns

Six flow patterns were observed: stratified-wavy (*SW*), stratified-smooth (*SS*), intermittent flow (*I*), churn flow (*C*), annular flow (*A*) and falling film flow (*F*), see photos in Fig. 10. These flow pattern characteristics can be found in two-phase flow references such as Taitel and Dukler (1976) and Taitel et al. (1980). In this study, the stratified-smooth (*SS*) flow was defined when the liquid layer height signal was stable; when the liquid layer thickness signal became oscillating, the stratified-wavy (*SW*) flow was named. The intermittent flow (*I*) was defined when the wave crest of the stratified-wavy flow reached the top of tube wall. The *SW* and *I* flows involved apparent interface waves, which will be further explained. The bubbly flow and slug flow (Taylor bubbles) were not observed, due to the less importance of the surface tension force. The falling film flow took place for the vertical downflow, involving thicker liquid film on the wall in contrast to the annular flow.

Fig. 11 shows flow pattern maps at the five inclination angles of $\theta = 0°$, $-15°$, 15°, $-90°$ and 90°. The data points and transition boundaries (dashed curves) were illustrated. For the horizontal flow (see Fig. 11a), the *SW*, *I* and *A* flows were observed with a narrow range of the intermittent flow. For the comparison purpose,

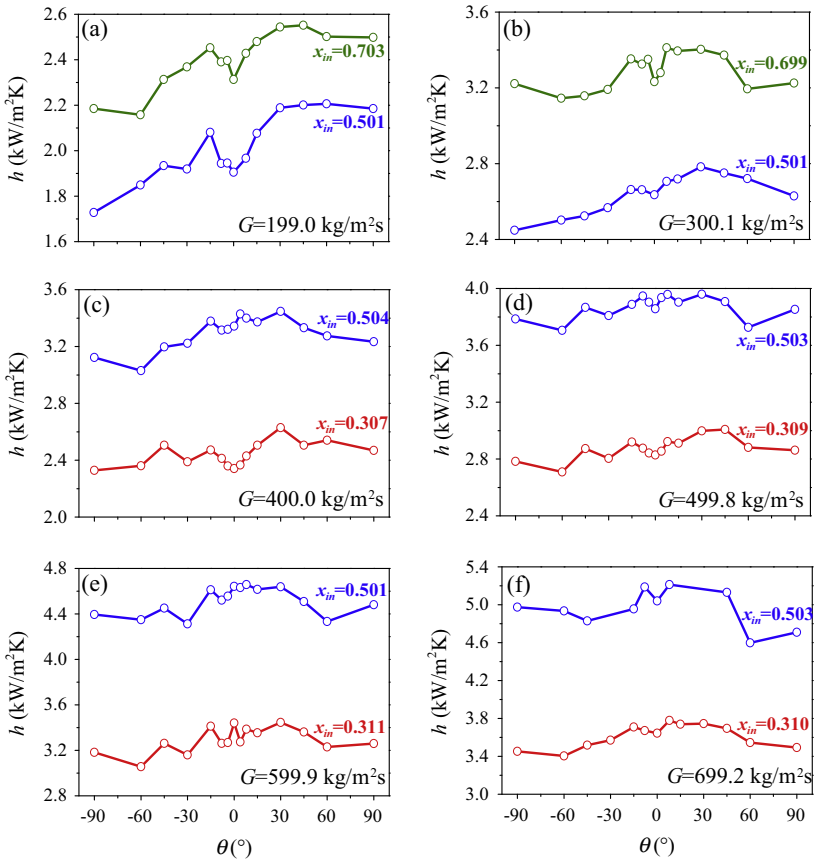

Fig. 7. Effect of inclination angles on the condensation heat transfer coefficients.

Fig. 11a plotted the transition boundaries by Hajal et al. (2003). Since the mass fluxes of R245fa in this study were more than 190 kg/m^2 s, the stratified-smooth flow was not observed in the horizontal tube, which is consistent with the flow pattern map predicted by Hajal et al. (2003).

Fig. 11b and c compared flow pattern maps between $\theta = -15°$ and $\theta = 15°$. For the inclined downflow ($\theta = -15°$), the gravity force has a positive component on the axial coordinate, accelerating the liquid flow to minimize the liquid height over the tube cross section. The flow was more stable thus the stratified-smooth (*SS*) flow appears in the left-bottom corner in Fig. 11b. The stratified-wavy (*SW*) flow only occurs when the mass fluxes are large enough to cause the interface wave at the vapor–liquid interface. Therefore, the *SS*, *SW* and *A* flows are the flow patterns with $\theta = -15°$, in which the annular flow (*A*) takes place at higher vapor mass qualities such as $x > 0.3$–0.4. On the other hand, the inclined upflow causes negative gravity force component on the axial coordinate, yielding higher liquid heights in the tube. Because the shear stress on the vapor–liquid interface is opposite to the gravity force component on the axial coordinate, the interface becomes more unstable. Thus, the stratified-smooth (*SS*) flow was not observed in Fig. 11c. Instead, the stratified-wavy (*SW*) flow appeared in the left-bottom corner in Fig. 11c (Barnea et al., 1985). Because the liquid volume fraction over the tube cross section is large enough, the "accumulated" liquid forms the liquid bridge to yield the intermittent (*I*) flow in a larger area (see Fig. 11c) (Taitel and Dukler, 1976). The annular (*A*) flow also takes place at higher vapor mass qualities.

Fig. 11d and e compared flow pattern maps for $\theta = -90°$ and $\theta = 90°$. For the vertical downflow, the shear stress on the vapor–liquid interface is decreased due to the buoyancy force of the vapor phase in the tube. Thus, thick liquid films are formed on the tube wall to yield the falling film (*F*) flow. However, for the vertical upflow, the shear stress at the vapor–liquid interface is maximized to cause the flow more chaotic. Thus, the churn (*C*) flow covered a larger area in Fig. 11e.

Because the surface tension force of R245fa is small and the tube diameter is relatively large, bubbly flow and slug flow were not observed in this study. Flow patterns here are mainly governed by the gravity force and inertia force.

The vapor–liquid interface

In addition to flow pattern observations, we also identified the interface wave. Later we will see that the interface wave is one of the reasons to yield the non-monotonic behavior of condensation heat transfer coefficients with inclination angles. The major flow patterns in the condenser tube were *SS*, *SW* and *I* except for the vertical flows. It is noted that, even though some cases of this study did contain annular flow at the condenser inlet, the flow was quickly evolved to other flow patterns such as *SS*, *SW* or *I*. This is because the annular flow had much higher condensation heat transfer coefficients at the tube entrance compared with other flow patterns. The flow length for the annular flow is significantly short compared with the whole condenser length. Thus, the annular flow analysis was paid less attention here.

The dynamic liquid films at the tube top and bottom were acquired using the high speed videos by analyzing the gray gradient of videos. The similar method was reported by Ong and Thome (2011). The MATLAB software was used to process the video images to detect the liquid–vapor interface and channel wall, which were determined based on the number of image pixels. Fig. 12 shows the image processing principle. The algorithm detected the liquid–vapor interface by locating the pixel which had the peak gradient in light intensity in the vertical direction.

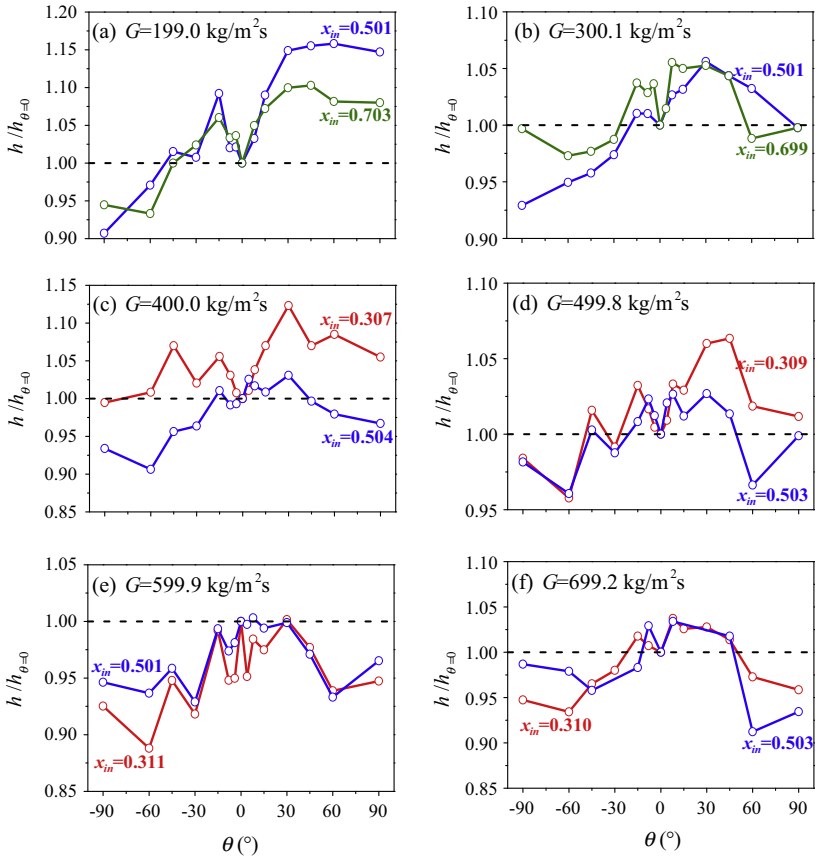

Fig. 8. Effect of inclination angles on $h/h_{\theta=0}$.

At first, the raw images were converted into a gray scale image (intensity images) that contains intensity values in the range of 0–255. A two-dimensional Gaussian low-pass filter was applied to smooth the image and reduce the image noise. The convolution was performed as two one-dimensional sums. The filtering was achieved by an averaging operation where the values come from each term divided by the sum of all terms in the kernel. Two 1×3 filters, one applied horizontally and one vertically and a standard deviation, $S_x = 2$ pixels was applied to smooth the images. The images were then processed to determine the intensity gradient in the vertical Y-direction corresponding to a given pixel coordinate, X, to detect the liquid-wall boundaries and liquid–vapor interfaces by locating the peak in the maximum and minimum values from the image gradient data.

The processed data identified the non-monotonic behavior of condensation heat transfer coefficients with respect to inclination angles. Fig. 13 shows the three cases with the same mass flux of $G = 199.0$ kg/m^2 s and $x = 0.307$. The inclination angles were $-8°$, $0°$ and $8°$, respectively. The original video images show the stratified flow at $\theta = 8°$ and $0°$. The liquid height at $\theta = -8°$ was slightly lower than that at $\theta = 0°$ (see Fig. 13a and b). Fig. 13c shows the significant variation of liquid heights versus time. The large amplitude wave appeared with the wave crest traveling downstream versus time. In order to characterize the liquid height oscillation, the dimensionless liquid height (h_l/d_i) and standard deviation of the dimensionless liquid height (σ_l) were defined as follows:

$$(h_l/d_i)_{ave} = \frac{1}{n}\sum_{1}^{n}(h_l/d_i) \tag{15}$$

$$\sigma_l = \left\{\frac{\sum_1^n [h_l/d_i - (h_l/d_i)_{ave}]^2}{n-1}\right\}^{1/2} \tag{16}$$

where the subscript *ave* means the average value and n referred to the number of data samples. The bottom wall and top wall corresponded to $h_l/d_i = 0$ and 1, respectively, d_i was the inner tube diameter. The larger the standard deviation of h_l/d_i, the more unstable the liquid–vapor interface was.

Fig. 14 shows the processed h_l/d_i signal versus time at the three inclination angles. The cases were exactly identical to those shown in Fig. 13. At $\theta = -8°$, $(h_l/d_i)_{ave}$ was 0.305. The signal was quasi-stable and the standard deviation of h_l/d_i was as low as 0.032 (see Fig. 14a). The horizontal position ($\theta = 0°$) yielded slightly higher liquid height of $h_l/d_i = 0.358$ with small standard deviation of 0.047 (see Fig. 14b), noting that σ_l was slightly larger than that at $\theta = -8°$. Attention was paid to the inclined upward flow (see Fig. 14c). The average dimensionless liquid height was 0.367, which was the largest among the three inclination angles. But the signal was very unstable and behaved the chaotic characteristic with the stand deviation of h_l/d_i up to 0.107. It is mentioned that the stable liquid–vapor interface referred to the "quasi-stable interface". Even for the slightly inclined downflow of $\theta = -8°$, the liquid height signal behaved very small amplitude oscillations, but not "absolute stable interface" (see Fig. 14a). The mass and momentum exchange at the vapor–liquid interface is the disturbance source. For example, when liquid drops entrained in the vapor phase impacted the vapor–liquid interface, small disturbance occurs on the interface.

The liquid–vapor interface instability was enhanced by decreasing the vapor mass qualities. Fig. 15 shows the three cases with the vapor mass quality of 0.108. The three cases were identical to those in Figs. 13 and 14, but x was decreased. The interface wave was extended to the horizontal position ($\theta = 0°$, see Fig. 15b). The liquid–vapor interface instability was more violent at $\theta = 8°$, compared with that shown in Figs. 13 and 14. The wave crest reached

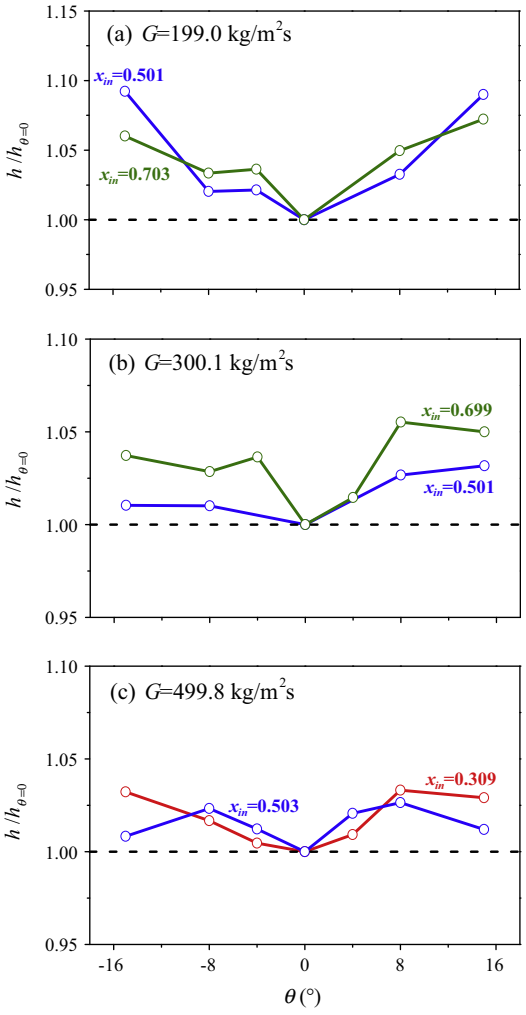

Fig. 9. $h/h_{\theta=0}$ at slight inclination angles.

the top wall surface. Both the present work and Lips and Meyer (2012a) classified the pattern shown in Fig. 15c as the intermittent flow. Fig. 16 shows the dimensionless liquid height signal. Both the signals at $\theta = 0°$ and 8° were greatly changed versus time. At $\theta = 8°$, the h_l/d_i dynamically reached 1, corresponding to the wave crest touching the top wall. The observed liquid layer thickness and interface wave explained the non-monotonic behavior of h with respect to θ.

Explanation of the observed data trend and phenomena

Here we started from the non-dimensional parameter analysis to show the present problem governed by inertia force, gravity force and Froude number. We tried to establish the connections among the flow patterns, interface wave and condensation heat transfer linked by the non-dimensional parameters. These parameters are (Dobson, 1994):

$$Fr = \frac{G^2}{\rho_f^2 g d_i} \tag{17}$$

$$Fr_f = \frac{G^2(1-x_{ave})^2}{\rho_f^2 g d_i} \tag{18}$$

$$Fr_g = \frac{G^2 x_{ave}^2}{\rho_g^2 g d_i} \tag{19}$$

$$X_{tt} = \left(\frac{1-x_{ave}}{x_{ave}}\right)^{0.9}\left(\frac{\rho_g}{\rho_f}\right)^{0.5}\left(\frac{\mu_f}{\mu_g}\right)^{0.1} \tag{20}$$

$$Bd = \frac{g(\rho_f-\rho_g)d_i}{\sigma} \tag{21}$$

$$We = \frac{G^2 d_i}{\rho_f \sigma} \tag{22}$$

where Fr, Fr_f, Fr_g, X_{tt}, Bd and We are the Froude number, Froude number of liquid phase, Froude number of vapor phase, Martinelli number, Bond number and Weber number, respectively. The subscripts of f and g are liquid and vapor, respectively. The symbols of ρ, μ and σ are density, viscosity and surface tension force, g is the gravity acceleration.

Flow pattern	Parameters	Photos
Stratified-wavy (SW)	G =199.0 kg/m²s x =0.108 θ =0°	
Stratified-smooth (SS)	G =196.9 kg/m²s x =0.104 θ =−15°	
Intermittent flow (I)	G =399.9 kg/m²s x =0.054 θ =15°	
Churn flow (C)	G =400.0 kg/m²s x =0.049 θ =90°	
Falling film (F)	G =300.3 kg/m²s x =0.109 θ =−90°	
Annular flow (A)	G =401.4 kg/m²s x =0.399 θ =90°	

Fig. 10. The observed flow patterns (the flow was from left to right).

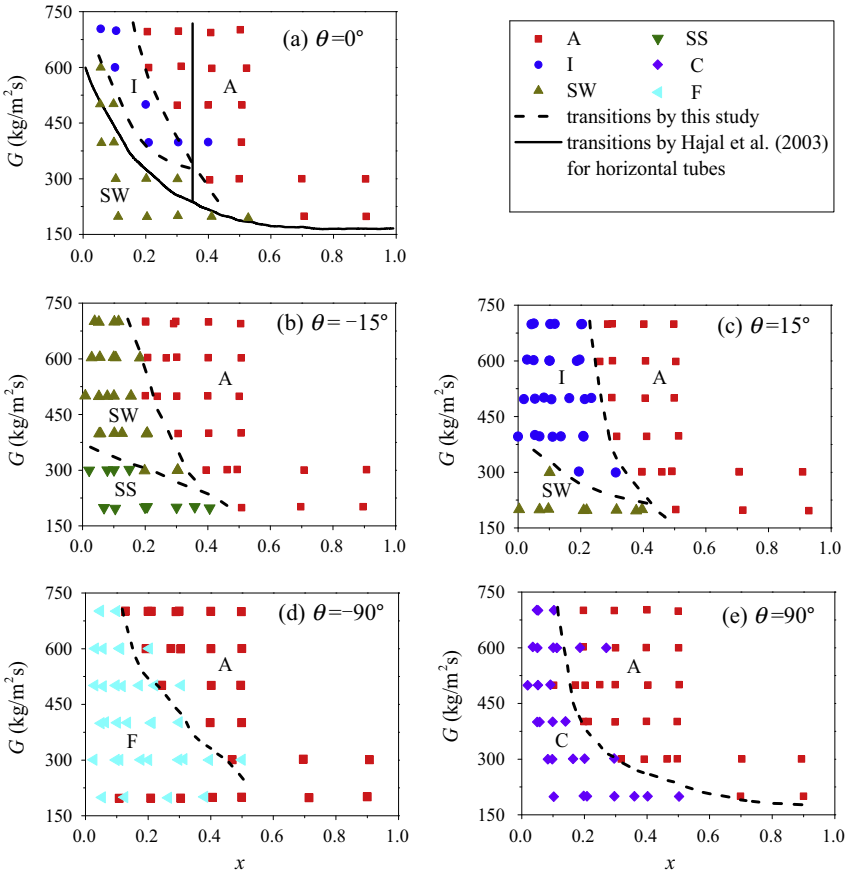

Fig. 11. Flow pattern maps at the five inclination angles (*A*: Annular flow, *C*: Churn flow, *F*: Falling film flow, *I*: Intermittent flow, *SS*: Stratified-smooth flow, *SW*: Stratified-wavy flow).

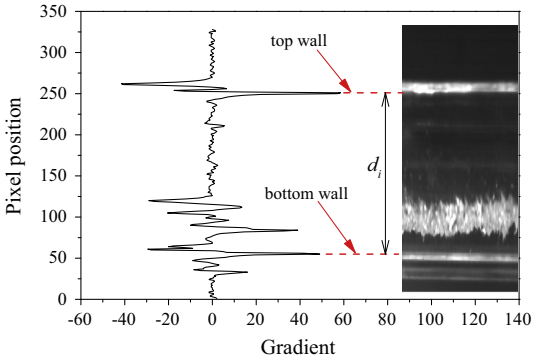

Fig. 12. The gray dependent interface capturer method.

Section 'Test section' described the experimental data ranges. Corresponding to the present data ranges, the Froude number was in the range of 0.174–2.153, indicating that both the inertia force and gravity force play important roles on condensation heat transfer. The Bond number was 17,554, indicating the negligible surface tension effect compared with the buoyancy force due to the density difference between the two-phases. The Weber number was in the range of 47–571, indicating the less importance of surface tension force compared with inertia force.

Flow patterns influenced by inertia force and gravity force

Inertia force influences the shear stress on the tube wall and the vapor–liquid interface. When the condenser was positioned at different inclination angles, the gravity force component on the axial coordinate will be changed to affect velocities within liquid layer and the shear stress due to the varied velocity difference between the two-phases. The inertia force and gravity force influence flow patterns in the following three respects. First, due to varied gravity force component on the axial coordinate, flow patterns are apparently different at different inclination angles (see Fig. 11). For example, *SW*, *I* and *A* flow patterns occur for the horizontal flow. But *F* and *A* flow patterns appeared for the vertical downflow. Second, the inclined upflow had negative gravity force component on the axial coordinate to decrease velocities of liquid phase. Thus, the liquid void fraction is larger but the vapor void fraction is smaller to accelerate the vapor phase. Thus the shear stress on the vapor–liquid interface is increased to result in more unstable interface nature. The inclined downflow became more stable. Third, the non-importance of surface tension force causes disappearance of bubbly flow and slug flow in this study.

Interface wave influenced by inertia force and gravity force

Interface waves may be accompanied with the stratified flow for inclined upflow (see section 'The flow patterns and interface wave'). The inclined upflow holds negative gravity force component on the axial coordinate. This effect slows down the liquid phase and speeds up the vapor phase to yield larger velocity difference between the two-phases. Thus, the shear stress on the vapor–liquid interface is increased to cause more unstable interface. When the inclination angles approach the vertical upflow, the churn or annular flow occurs thus the interface wave is not observed. The inclined downflow is more stable.

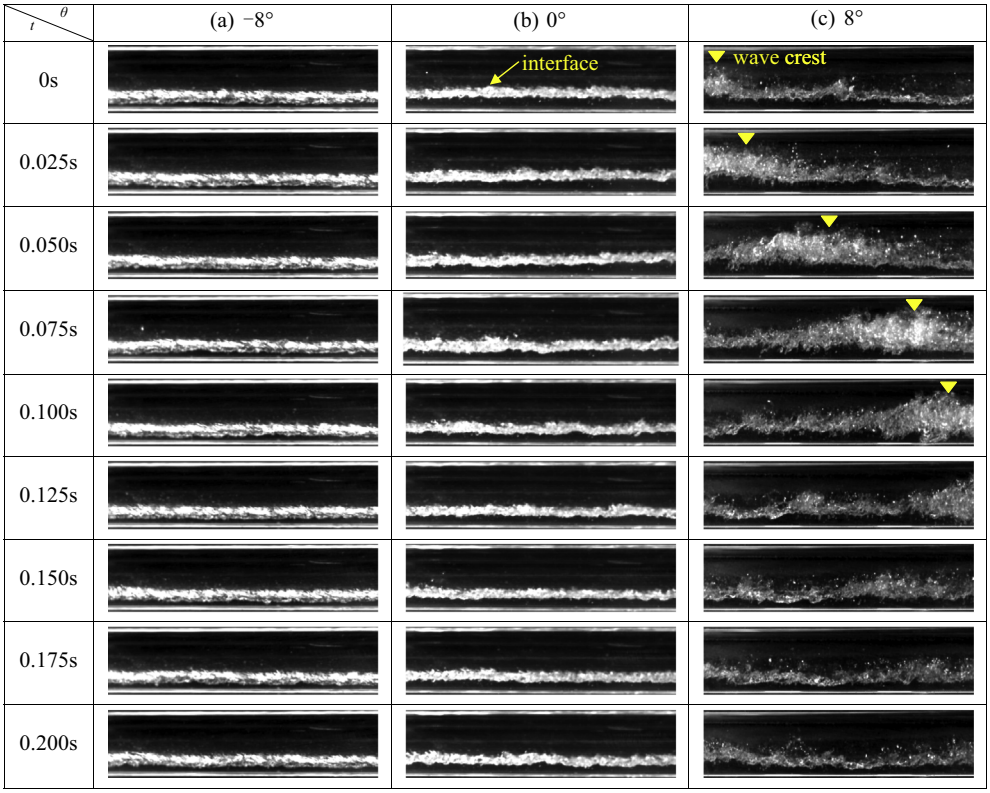

Fig. 13. The dynamic interfaces at the inclination angles of 0° and ±8° (G = 199.0 kg/m^2 s, x = 0.307).

Connections of flow patterns, interface wave and condensation heat transfer

Three key points should be paid great attention here: the general increase trend of condensation heat transfer coefficients in the full θ range, the non-monotonic behavior of heat transfer coefficients, and the special phenomenon related to small inclination angles.

It is known that flow patterns have strong connection with the heat transfer. Due to the combined effect of inertia force and gravity force, the inclined upflow displays unstable nature but the inclined downflow displays stable or quasi-stable nature. The disturbance of the interface can enhance heat transfer. This explains the general increase trend of condensation heat transfer coefficients, from the whole inclination angle range point of view.

The non-monotonic behavior of heat transfer coefficients can be explained by the competing balance between the liquid layer thickness and intensity of the interface wave. For the inclined upflow, the liquid layer thickness is increased by increasing the inclination angles, deteriorating the condensation heat transfer. On the other hand, the increased shear stress on the vapor–liquid interface causes more unstable interface, enhancing the condensation heat transfer. Thus, there is an optimal inclination angle at which the condensation heat transfer coefficients attained maximum. Such inclination angle was about 30° in this study. Beyond the optimal inclination angle, the interface wave maybe disappeared. Instead, the condenser tube was switched to other flow patterns. Thus, the intensity of interface wave is weakened to decrease the condensation heat transfer. Therefore, the non-monotonic behavior of condensation heat transfer coefficients takes place. For the inclined downflow, the condensation heat transfer coefficients are balanced by the liquid film thickness and buoyancy force between the two-phases. The non-monotonic behavior of heat transfer coefficients for the inclined downflow cases is more complicated and needs further investigation.

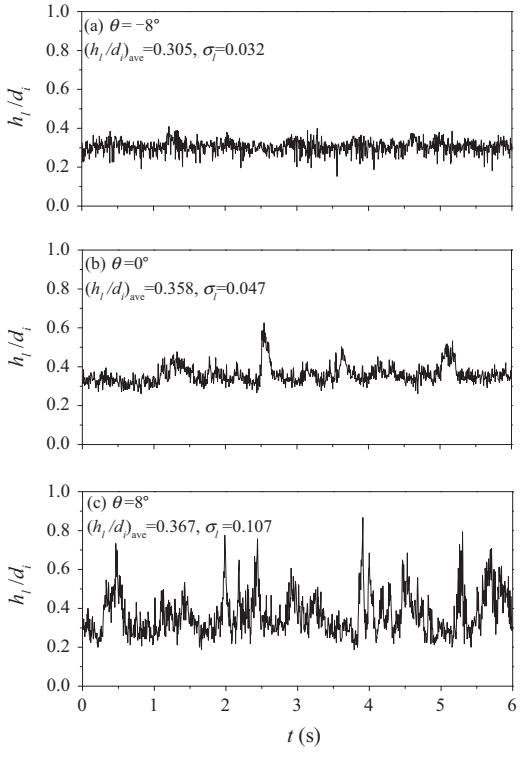

Fig. 14. The liquid height signal versus time at G = 199.0 kg/m^2 s and x = 0.307.

Fig. 9 shows that in a narrow θ range, the horizontal position had minimal condensation heat transfer coefficients. The heat transfer coefficients are sensitive to inclination angles at small θ. For the slightly inclined upflow, the interface wave is enhanced

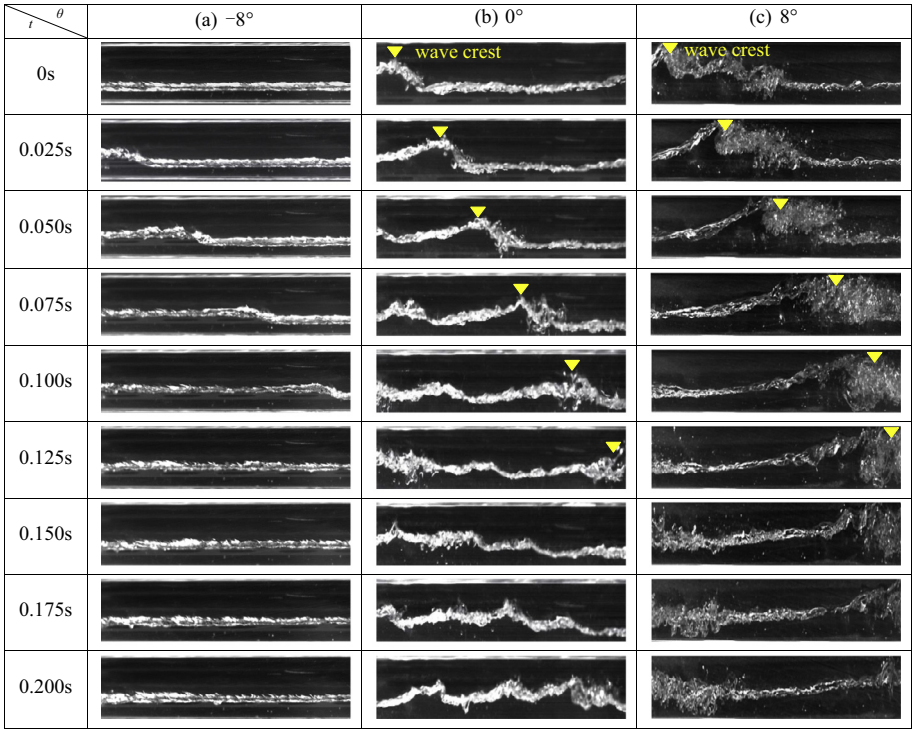

Fig. 15. The dynamic interfaces at inclination angles of 0° and ±8° (G = 199.0 kg/m^2 s, x = 0.108).

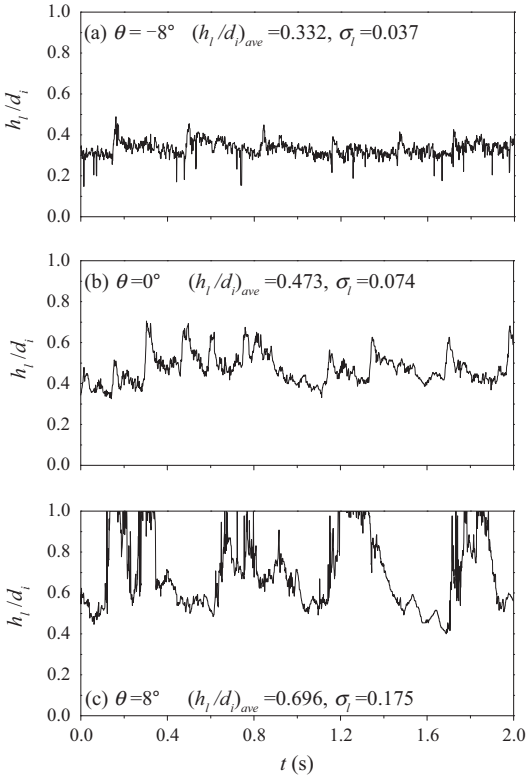

Fig. 16. The dynamic liquid height signal versus time (G = 199.0 kg/m^2 s, x = 0.108).

to have larger heat transfer coefficients than those at the horizontal position. For the slightly inclined downflow, the liquid layer thickness is decreased to have larger heat transfer coefficients than those at the horizontal position.

The two-step correlation of h with respect to θ

Here we compared our condensation heat transfer coefficients with the available correlations in the literature. It was found that heat transfer coefficients matched the Shah (2009) correlation well for the horizontal position. But large deviation between measured heat transfer coefficients and other correlations existed for inclined angles. Thus, a new correlation was developed. The correlations of Shah (2009), Dobson (1994), Thome et al. (2003) and Würfel et al. (2003) were selected (see Table 2 for detailed expressions). The following deviation parameters were defined:

$$e = \frac{h_{pre} - h_{\exp}}{h_{\exp}} \times 100\% \tag{23}$$

$$e_R = \frac{1}{n}\sum_{1}^{n}\left[\frac{h_{pre} - h_{\exp}}{h_{\exp}}\right] \times 100\% \tag{24}$$

$$e_A = \frac{1}{n}\sum_{1}^{n}\left[\frac{|h_{pre} - h_{\exp}|}{h_{\exp}}\right] \times 100\% \tag{25}$$

$$\sigma_n = \left\{\left[\sum_{1}^{n}(e - e_R)^2\right] \Big/ (n-1)\right\}^{1/2} \times 100\% \tag{26}$$

where e referred to the deviation, e_R, e_A, σ_n means the average deviation, mean absolute deviation and standard deviation, respectively, n was the number of data samples. The smaller the deviations, the more accurate of these correlations are to match the experimental data.

The experimental data at the horizontal position matched the correlations of Shah (2009) and Dobson (1994) well (see Fig. 17a and b). The three deviations of e_R, e_A and σ_n were less than 6%, in which negative and positive e_R values mean the experimental data smaller and larger than the predictions, respectively. The match of condensation heat transfer coefficients at the horizontal position with the Shah (2009) correlation further verified that the non-condensable gas effect is weak in this study. The Thome et al. (2003) correlation did not match the experimental data well, with the

Table 2
The correlation of condensation heat transfer coefficient.

Author and year	Correlations for heat transfer coefficient	Flow regime	Orientation
Shah (2009)	$h = h_{fo}(\mu_f/14\mu_g)^n[(1-x)^{0.8} + 3.8x^{0.76}(1-x)^{0.38}/p_{reduced}^{0.38}]$, $h_{fo} = k_f(0.023\mathrm{Re}_{fo}^{0.8}\mathrm{Pr}_f^{0.4})/d_i$ $n = 0.0058 + 0.557p_{reduced}$, $\mathrm{Re}_{fo} = Gd_i/\mu_f$	Annular, wavy intermittent	−90° to 0°, 90°
Dobson (1994)	Annular : $Nu = 0.023\mathrm{Re}_f^{0.8}\mathrm{Pr}_g^{0.4}\left[1+\frac{2.22}{X_{tt}^{0.89}}\right]$; Wavy : $Nu = \frac{0.2\mathrm{Re}_{go}^{0.12}}{1+1.11X_{tt}^{0.58}}\left[\frac{GaPr_f}{Ja}\right]^{0.25} + (1-\frac{\varphi}{2\pi})Nu_{forced}$ $Nu_{forced} = 0.0195\mathrm{Re}_f^{0.8}\mathrm{Pr}_g^{0.4}\sqrt{1.376 + c_1/X_{tt}^{c_2}}$, $Ja = C_{p,f}(T_{sat}-T_w)/i_{fg}$, $\mathrm{Re}_f = G(1-x)d_i/\mu_f$ $Ga = g\rho_f(\rho_f-\rho_g)d_i^3/\mu_f^2$, $(1-\varphi/2\pi) \cong \arccos(2\alpha-1)/\pi$, $\mathrm{Re}_{go} = Gd_i/\mu_g$ For $0 < Fr_f \leqslant 0.7, c_1 = 4.172 + 5.48Fr_f - 1.564Fr_f^2, c_2 = 1.773 - 0.169Fr_f$ For $Fr_f > 0.7, c_1 = 7.242, c_2 = 1.655$	Annular, wavy	0°
Thome et al. (2003)	$h = \frac{h_f\varphi+(2\pi-\varphi)h_c}{2\pi}$, $h_c = 0.003\mathrm{Re}_\delta^{0.74}\mathrm{Pr}_f^{0.5}\frac{k_f}{\delta}f_i$, $h_f = 0.728[\frac{\rho_f(\rho_f-\rho_g)gi_{fg}k_f^3}{\mu_f d_i(T_{sat}-T_w)}]^{1/4}$ $f_i = 1 + (u_g/u_f)^{1/2}((\rho_f-\rho_g)g\delta^2/\sigma)^{1/4}$, $\mathrm{Re}_\delta = 4G(1-x)\delta/[(1-\alpha)\mu_f]$	Annular intermittent Stratified mist	0°
Würfel et al. (2003)	$Nu = a\mathrm{Re}_{film}^b(1+\tau)^c\mathrm{Pr}_L^d(1+\sin\theta)^{0.214}$, $\tau = f\Psi\rho_g u_g^2/(8\rho_f v_f^2/L^2)$, $f = 0.3414(1+80000\mathrm{Re}_{film}^{0.71}\mathrm{Re}_g^{-1.4})/\mathrm{Re}_g^{0.25}$ $\Psi = 2G(1-x)\pi d_i^2/fu_g\rho_g$, $L = (v_L^2/g)^{1/3}$, $u_g = Gx/\rho_g$, $\mathrm{Re}_{film} = G(1-x)d_i/4\mu_f$, $\mathrm{Re}_g = Gxd_i/\mu_g$ $a = 0.02536$, $b = 0.077$, $c = 0.501$, $d = 0.4$	Annular Annular-mist Stratified	0–90°

Note: The symbols δ, α, φ, u were liquid film thickness, void fraction, upper angle of the tube not wetted by stratified liquid and velocity, respectively.

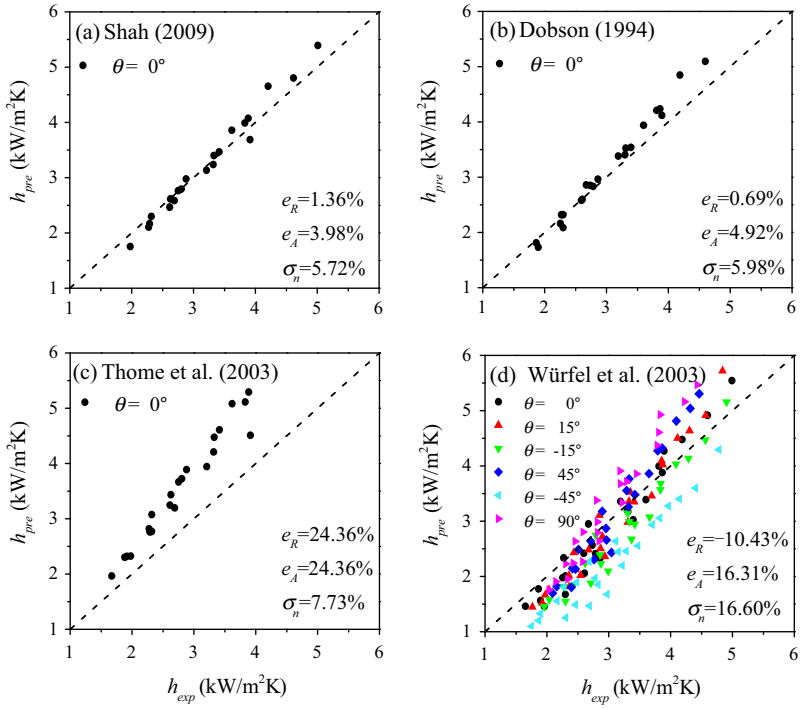

Fig. 17. The comparison between the measured condensation heat transfer coefficients and predictions using various authors' correlation.

deviations of e_R and e_A up to about 24% (see Fig. 17c). This was due to the overestimate of void fractions in the Hajal et al. (2003) model. Fig. 17d shows that the experimental data significantly deviated from the Würfel et al. (2003) correlation at various inclination angles, in which e_A and σ_n attained about 16%. This encouraged us to search a better correlation, which was given as

$$\frac{h}{h_{\theta=0}} = (1+a\theta)[1+b\sin(c\theta)] \tag{27}$$

There are three findings on the condensation heat transfer coefficients. First, the condensation heat transfer coefficients at a specific inclination angle deviated from that at the horizontal position. The parameter of $h/h_{\theta=0}$ in Eq. (27) reflects the deviation degree from that of horizontal flow. Second, the condensation heat transfer coefficients had a general rise trend versus θ in the full θ range. The term of $1 + a\theta$ in Eq. (27) represents the "general rise trend". Third, $h/h_{\theta=0}$ displays the non-monotonic behavior versus θ. Thus, the term of $1 + b\mathrm{Sin}(c\theta)$ in Eq. (27) represents the non-monotonic effect.

Fig. 18 shows the two-step correlation principle, in which Fig. 18a shows the non-monotonic behavior in a sine function (only the positive θ range was shown) and Fig. 18b shows the general increasing trend in the full θ range. Fig. 18c shows a satisfactory correlation by combining Fig. 18a and b. The parameters of a, b and c in Eq. (27) had specific physical meanings, with a representing the slope of $h/h_{\theta=0}$ with respect to θ (see Fig. 18b). The parameter b represented the non-monotonic variation amplitude to indicate how much of the heat transfer coefficient at θ deviating from that at $\theta = 0$. The parameter c determined the cycle number of $h/h_{\theta=0}$ in the full θ range.

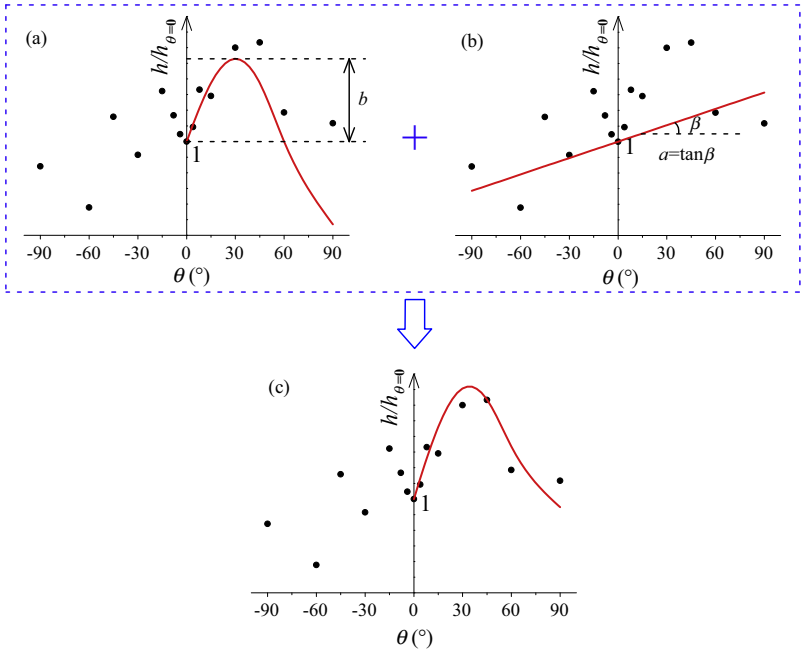

Fig. 18. The two-step correlation principle of the experimental data.

Table 3
The slope gradient a versus different parameters.

Fr	Fr_f	Fr_g	x_{ave}	X_{tt}	a
0.174	0.080	55.981	0.323	0.360	0.083
0.174	0.049	118.642	0.471	0.206	0.054
0.174	0.022	222.352	0.645	0.108	0.028
0.397	0.178	132.719	0.330	0.350	0.034
0.397	0.096	313.212	0.507	0.180	0.012
0.397	0.039	570.077	0.684	0.092	0
0.705	0.464	76.527	0.188	0.691	0.026
0.705	0.377	156.075	0.269	0.456	0.028
0.705	0.290	278.080	0.359	0.313	0.022
1.100	0.712	129.159	0.196	0.661	0.020
1.100	0.565	271.129	0.283	0.427	0.017
1.100	0.424	485.065	0.379	0.289	0.007
1.585	0.966	233.561	0.219	0.581	0.017
1.585	0.768	448.928	0.304	0.391	0.015
1.585	0.558	803.896	0.407	0.260	0.009
2.153	1.318	312.417	0.217	0.587	0.015
2.153	1.020	641.187	0.312	0.378	0.010
2.153	0.777	1053.259	0.399	0.268	0

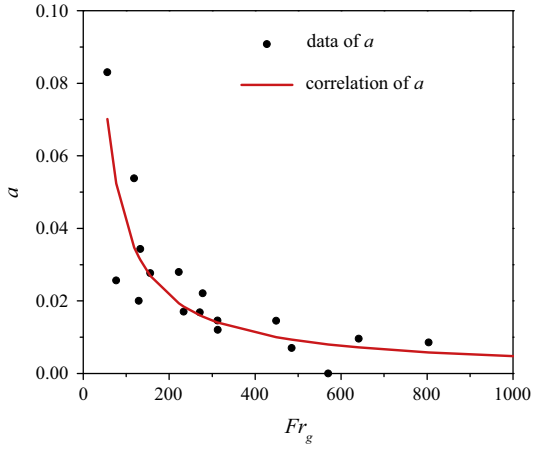

Fig. 19. The slope a versus Fr_g.

The determination of a: For a given combination of G and x_{in} (or x_{ave}), tests were performed with θ from $-90°$ to $90°$, yielding an a value of by linear correlation of $h/h_{\theta=0}$ versus θ (see Fig. 18b). Different combinations of G and x obtained different a values. Table 3 lists a values versus Fr, Fr_f, Fr_g, x_{ave}, X_{tt}. It was found that a can be well correlated with Fr_g (Froude number of the vapor phase). Fig. 19 shows the correlation, which is written as

$$a = \frac{3.024}{Fr_g^{0.935}} \tag{28}$$

Fig. 19 and Eq. (28) show that a was decreased with increases of Fr_g, meaning that the increase trend of $h/h_{\theta=0}$ versus θ was more apparent at smaller Fr_g (smaller G and/or x_{ave}). Larger G and/or x_{ave} weakened the increase trend of h versus θ (see Figs. 7 and 8).

The determination of b: The h $h_{\theta=0}$ attained two maximum values at $\theta = 30°$ and $-15°$. The b values represented the amplitude at the two angles (see Fig. 18a). Because the data trends were different for upward and downward flows, b was correlated for two separate θ ranges of ($-90°$ to $0°$) and (0–$90°$). For a specific combination of G and x_{ave}, there are two b values with one occurring at $\theta = 30°$ and the other occurring at $\theta = -15°$:

$$b = \frac{0.172}{Fr^{0.17}x_{ave}^{0.239}} - 0.197 \quad \text{for } 0° < \theta < 90° \tag{29}$$

$$b = \frac{0.024}{Fr^{0.584}x_{ave}^{0.654}} - 0.03 \quad \text{for } -90° < \theta < 0° \tag{30}$$

Eqs. (29) and (30) show that the non-monotonic variation amplitudes were decreased with increases in Fr and x_{ave}, consistent with the condensation heat transfer measurements well. Figs. 7 and 8 show larger deviations (b values) at $\theta = 30°$ and $-15°$ for lower mass fluxes and/or vapor mass qualities.

The determination of c: The c values should be decided so that $\sin(c\theta)$ is equal to 1 at $\theta = 30°$ and $-15°$. Therefore, c was equal to 6 for $-90° < \theta < 0°$ and 3 for $0° < \theta < 90°$, respectively.

Finally, the dimensionless parameter of $h/h_{\theta=0}$ was given as follows:

$$\frac{h}{h_{\theta=0}} = \left(1 + \frac{3.024\theta}{Fr_g^{0.935}}\right)\left\{1 + \left[\frac{0.172}{Fr^{0.17}x_{ave}^{0.239}} - 0.197\right]\sin(3\theta)\right\} \quad \text{for } 0^\circ < \theta < 90^\circ \tag{31}$$

$$\frac{h}{h_{\theta=0}} = \left(1 + \frac{3.024\theta}{Fr_g^{0.935}}\right)\left\{1 + \left[\frac{0.024}{Fr^{0.584}x_{ave}^{0.654}} - 0.03\right]|\sin(6\theta)|\right\} \quad \text{for } -90^\circ < \theta < 0^\circ \tag{32}$$

Fig. 20 shows the comparison between measured $h/h_{\theta=0}$ data and predictions by Eqs. (31) and (32). The correlations reflect the non-monotonic behavior of $h/h_{\theta=0}$ versus θ. The agreement in the full θ range was quite satisfactory, with maximum deviation of about 5%. Fig. 21 plots the comparison between predicted h and measured h, in which $h_{\theta=0}$ was predicted by Shah (2009) correlation in Fig. 21a and by Dobson (1994) correlation in Fig. 21b. Excellent agreement between them was reached. The three deviation parameters of e_R, e_A and σ_n were about 5–6%.

Fig. 22 shows measured pressure drops across the test section, noting that pressure drop included the frictional, accelerating and gravity pressure drop component. Attention was paid to the near horizontal position. Pressure drops were very sensitive to the subtle variation of inclination angles near the horizontal position. They always reached maximum value at the horizontal position, but they were sharply decreased when θ deviated from zero. The measurements of heat transfer and pressure drop suggested that condenser should be operated at $\theta = 30^\circ$ or -15°, because the two inclination angles not only had maximum heat transfer coefficients but also had smallest pressure drops. The exactly horizontal position was not ideal to operate the condenser.

In summary, the condensation heat transfer data and its correlation are useful for industrial applications. Due to the good comprehensive performance, R245fa fluid is strongly recommended to be used in heat pumps and Organic Rankine Cycles (Kang, 2012; Wang et al., 2011). The condensation heat transfer data of R245fa in this study is expected by various industry sectors. The effect of inclination angles on heat transfer coefficients provided the guideline to select "best inclination angle" for the condenser operation. In additional to these, the 14.81 mm diameter copper tube is a commercial tube (Lee et al., 2014).

The heat transfer correlation was based on the non-dimensional parameter analysis. The correlation is suitable when inertia force and gravity force are important but surface tension force is not important. This study covered the Froude number (Fr) range of (0.174–2.153). The Bond number (Bd) and Weber number (We) should be significantly larger than one ($Bd \gg 1$, $We \gg 1$), ensuring buoyancy force and inertia force significantly suppressing surface tension force effect.

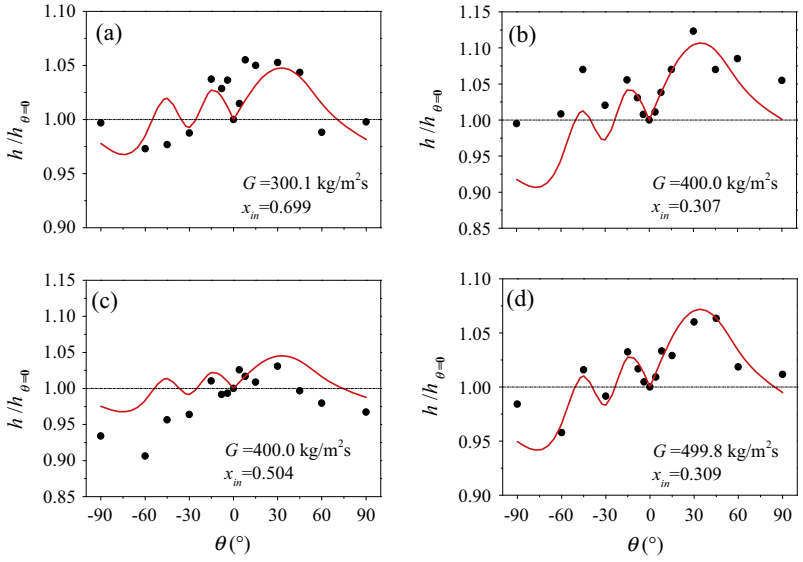

Fig. 20. The comparison between the measured $h/h_{q=0}$ and the new correlation's predictions.

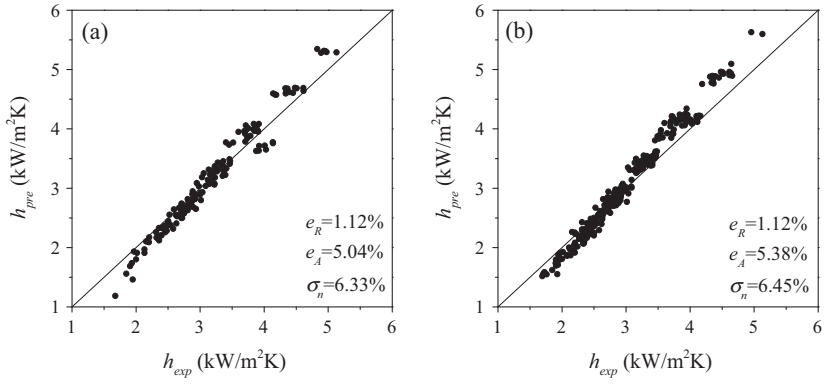

Fig. 21. The comparison between the measured condensation heat transfer coefficients and the new predictions, in which $h_{\theta=0}$ was computed by Shah (2009) in (a) and Dobson (1994) in (b).

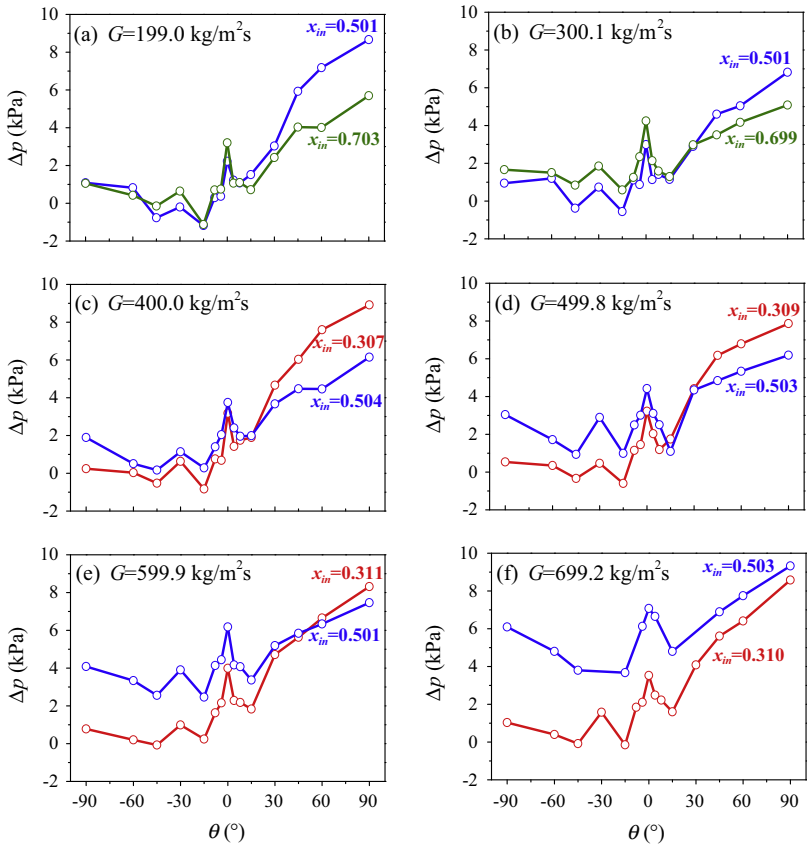

Fig. 22. The measured pressure drops versus inclination angles.

Even though the tube diameter was 14.81 mm and the organic fluid was R245fa, the correlation is expected to be used for other tube diameters and organic fluids, if *Fr* lied in the range of (0.174–2.153) and *Bd* and *We* are significantly larger than one. The correlation should be further verified if *Fr*, *Bd* and *We* are beyond the recommended range. It is certain that the correlation should be suitable for larger tube diameter than 14.81 mm. Larger tube diameter yields larger *Bd* and *We* number. Also due to the non-dimensional analysis, the correlation is expected to be taken as the reference for other organic fluids.

Conclusions

The following conclusions can be drawn:

- The present data identified the importance of inertia force and gravity force. But surface tension force is not important to affect condensation heat transfer.
- The condensation heat transfer coefficients showed the general increase trend versus inclination angles and the non-monotonic behavior in the full inclination angle range.
- The condensation heat transfer coefficients were sensitive to inclination angles near the horizontal positions. The slightly inclined positions (either upward or downward) enhances condensation heat transfer.
- Flow patterns mainly included stratified-smooth flow, stratified-wavy flow and intermittent flow. Annular flow at the condenser inlet quickly evolved into other flow patterns. Bubbly flow and slug flow were not observed.
- Flow patterns and interface waves explained the heat transfer trend linked by the Froude number. The liquid layer thickness and interface wave competed with each other to influence condensation heat transfer coefficients for inclined upflow. An optimal inclination angle exists to reach maximum heat transfer coefficient. The inclined downward flow is more stable and heat transfer coefficients are balanced by the liquid layer thickness and buoyancy force.
- A new correlation of condensation heat transfer coefficients was developed with the non-dimensional parameter analysis. The correlation well correlated the Froude number and vapor mass qualities.
- The condenser was suggested to be operated at the inclination angles of −15° or 30°. The exactly horizontal position decreases condensation heat transfer coefficients and increases pressure drops.

Acknowledgements

This work was supported by the Natural Science Foundation of China (51436004, 51210011) and the National Basic Research Program of China (2011CB710703).

References

Barnea, D., Shoham, O., Taitel, Y., Dukler, A.E., 1985. Gas-liquid flow in inclined tubes: flow pattern transitions for upward flow. Chem. Eng. Sci. 40 (1), 131–136.

Caruso, G., Vitale, D.M.D., Naviglio, A., 2013. Condensation heat transfer coefficient with noncondensable gases inside near horizontal tubes. Desalination 309, 247–253.

Dalkilic, A.S., Wongwises, S., 2009. Intensive literature review of condensation inside smooth and enhanced tubes. Int. J. Heat Mass Transf. 52, 3409–3426.

Dittus, F.W., Boelter, L.M.K., 1985. Heat transfer in automobile radiators of the tubular type. Int. Commun. Heat Mass Transfer 12, 3–22.

Dobson, M.K., 1994. Heat transfer and flow regimes during condensation in horizontal tubes. Air Conditioning and Refrigeration Center. College of Engineering. University of Illinois at Urbana-Champaign.

Frisk, D.P., Davis, E.J., 1972. The enhancement of heat transfer by waves in stratified gas-liquid flow. Int. J. Heat Mass Transf. 15, 1537–1552.
Gupta, R., Fletcher, D.F., Haynes, B.S., 2010. Taylor flow in microchannels: a review of experimental and computational work. J. Comput. Multiphase Flows 2, 1–32.
Hajal, J.E., Thome, J.R., Cavallini, A., 2003. Condensation in horizontal tubes, Part 1: Two-phase flow pattern map. Int. J. Heat Mass Transf. 46, 3349–3363.
Holman, J.P., Gajda, W.J., 1994. Experimental Methods for Engineers, vol. 2. McGraw-Hill, Nueva York.
Jayanti, S., Hewitt, G.F., 1996. Hydrodynamics and heat transfer of wavy thin film flow. Int. J. Heat Mass Transf. 40, 179–190.
Kang, S.H., 2012. Design and experimental study of ORC (organic Rankine cycle) and radial turbine using R245fa working fluid. Energy 41, 514–524.
Kattan, N., Thome, J.R., Favrat, D., 1998. Flow boiling in horizontal tubes: Part 1—Development of a diabatic two-phase flow pattern map. J. Heat Transfer 120 (1), 140–147.
Laohalertdecha, S., Wongwises, S., 2010. The effects of corrugation pitch on the condensation heat transfer coefficient and pressure drop of R-134a inside horizontal corrugated tube. Int. J. Heat Mass Transf. 53, 2924–2931.
Lee, H.S., Yoon, J.I., Kim, J.D., Bansal, P.K., 2006. Condensing heat transfer and pressure drop characteristics of hydrocarbon refrigerants. Int. J. Heat Mass Transf. 49 (11), 1922–1927.
Lee, Y.R., Kuo, C.R., Liu, C.H., Fu, B.R., Hsieh, J.C., Wang, C.C., 2014. Dynamic response of a 50 kW organic rankine cycle system in association with evaporators. Energies 7 (4), 2436–2448.
Lips, S., Meyer, J.P., 2011. Two-phase flow in inclined tubes with specific reference to condensation: a review. Int. J. Multiph. Flow 37, 845–859.
Lips, S., Meyer, J.P., 2012a. Experimental study of convective condensation in an inclined smooth tube. Part I: Inclination effect on flow pattern and heat transfer coefficient. Int. J. Heat Mass Transf. 55, 395–404.
Lips, S., Meyer, J.P., 2012b. Stratified flow model for convective condensation in an inclined tube. Int. J. Heat Fluid Flow 36, 83–91.
Madhawa, H.H.D., Golubovic, M., Worek, W.M., Ikegami, Y., 2007. Optimum design criteria for an organic Rankine cycle using low-temperature geothermal heat sources. Energy 32, 1698–1706.
Mohseni, S.G., Akhavan-Behabadi, M.A., Saeedinia, M., 2013. Flow pattern visualization and heat transfer characteristics of R-134a during condensation inside a smooth tube with different tube inclinations. Int. J. Heat Mass Transf. 60, 598–602.
Nikuradse, J., 1950. Laws of flow in rough pipes. National Advisory Committee for Aeronautics, Washington.
Ong, C.L., Thome, J.R., 2011. Macro-to-microchannel transition in two-phase flow: Part 1 – Two-phase flow patterns and film thickness measurements. Exp. Thermal Fluid Sci. 35, 37–47.
Saffari, H., Naziri, V., 2010. Theoretical modeling and numerical solution of stratified condensation in inclined tubes. J. Mech. Sci. Technol. 24 (12), 2587–2596.
Schuster, A., Karellas, S., Kakaras, E., Spliethoff, H., 2009. Energetic and economic investigation of organic Rankine Cycle applications. Appl. Therm. Eng. 29, 1809–1817.
Shah, M.M., 2009. An improved and extended general correlation for heat transfer during condensation in plain tubes. HVAC&R Res. 15 (5), 889–891.
Son, C.H., Oh, H.K., 2012. Condensation heat transfer characteristics of CO_2 in a horizontal smooth-and microfin-tube at high saturation temperatures. Appl. Therm. Eng. 36, 51–62.
Taitel, Y., Dukler, A.E., 1976. A model for predicting flow regime transitions in horizontal and near horizontal gas-liquid flow. AIChE J. 22, 47–55.
Taitel, Y., Bornea, D., Dukler, A.E., 1980. Modelling flow pattern transitions for steady upward gas-liquid flow in vertical tubes. AIChE J. 26, 345–354.
Thome, J.R., Hajal, J.E., Cavallini, A., 2003. Condensation in horizontal tubes, part 2: new heat transfer model based on flow regimes. Int. J. Heat Mass Transf. 46, 3365–3387.
Tropea, C., Yarin, A.L., Foss, J.F., 2007. Springer Handbook of Experimental Fluid Mechanics, vol. 1. Springer.
Vinš, V., Hrubý, J., 2011. Solubility of nitrogen in one-component refrigerants: prediction by PC-SAFT EoS and a correlation of Henry's law constants. Int. J. Refrig. 34 (8), 2109–2117.
Wang, B.X., Du, X.Z., 2000. Study on laminar film-wise condensation for vapor flow in an inclined small/mini-diameter tube. Int. J. Heat Mass Transf. 43, 1859–1868.
Wang, E.H., Zhang, H.G., Fan, B.Y., Ouyang, M.G., Zhao, Y., Mu, Q.H., 2011. Study of working fluid selection of organic Rankine cycle (ORC) for engine waste heat recovery. Energy 36, 3406–3418.
Wang, W.C., Ma, X.H., Wei, Z.D., Yu, P., 1998. Two-phase flow patterns and transition characteristics for in-tube condensation with different surface inclinations. Int. J. Heat Mass Transf. 41, 4341–4349.
Wei, D.H., Lu, X.S., Lu, Z., Gu, J.M., 2007. Performance analysis and optimization of organic Rankine cycle (ORC) for waste heat recovery. Energy Convers. Manage. 48, 1113–1119.
Weisman, J., Duncan, D., Gibson, J., Crawford, T., 1979. Effects of fluid properties and pipe diameter on two-phase flow patterns in horizontal lines. Int. J. Multiph. Flow 5, 437–462.
Würfel, R., Kreutzer, T., Fratzscher, W., 2003. Turbulence transfer processes in adiabatic and condensing film flow in an inclined tube. Chem. Eng. Technol. 26, 439–448.
Yang, C.Y., Shieh, C.C., 2001. Flow pattern of air–water and two-phase R-134a in small circular tubes. Int. J. Multiph. Flow 27, 1163–1177.